Modifying Strontium Optical Lattice Clock for Quantum Simulation

by

Daniel Reed

A thesis submitted to the University of Birmingham

for the degree of Master of Philosophy

School of Physics and Astronomy

Univeristy of Birmingham

July 2017

Acknowledgements

I truly enjoyed my time studying and working towards this MPhil. The learning curve has been incredibly steep and the new skills I have gained both technically and in terms of scientific thinking are worlds apart from when I completed my undergraduate studies in June 2015. This is due in no small part to the fantastic people who I have had the opportunity to surround myself with, and whose knowledge I have been able to soak up by osmosis.

My first thanks go to Professor Kai Bongs and Dr Yeshpal Singh who very kindly chose me to represent the University of Birmingham Cold Atom group at JILA, University of Colorado and to Professor Jun Ye who was kind enough to allow me into his world class lab.

Jun has a wealth of technical knowledge, an unbelievable experimental intuition and a passion for science that cannot fail to inspire. He always seems to ask the right questions when you are facing a technical problem to help you overcome the current hurdle so that you can 'get on and do science'. Our weekly group meetings were probably the highlight of my time at JILA. I was also lucky enough to get advice from time to time with the 'grand-father of the optical clock' Jan Hall. Jan's help is often oracular in nature and may require weeks or months to fully percolate, but is always extremely helpful.

I want to thank my Sr1 team-mates: Shimon Kolkowitz, Sarah Bromley and Toby Bothwell who all provided help, support and knowledge as well as being very welcoming when I first arrived. Also, our colleagues on Sr2 and Stable Lasers: Ed Marti, Akihisa Goban, Sara Campbell, Ross Hutson and Wei Zhang, Eric Oelker, Lindsay Sonderhouse and John Robinson who provided huge scientific and technical support, stimulating dinner company and willing table tennis opponents.

I feel incredibly lucky to have been able to spend a year in such esteemed company and whatever I do in the future will bear the hallmarks of the way my colleagues and friends taught me to think and to see the world.

Abstract

The Strontium Optical Lattice Clock at JILA has been at the forefront of optical metrology for a number of years. Recently, it has been proposed that this system could be used as a novel quantum simulator to study spin-orbit coupled fermions in the optical lattice using the extremely precise spectroscopic tool of the $^1S_0 \rightarrow {}^3P_0$ clock transition and ultra-narrow clock laser. This thesis gives an overview of the use of the lattice clock system as a quantum simulator and the lattice intensity control which was developed in order to enable the new experimental direction. It will also provide background for the results presented in the group's recent publication [1].

Contents

1 Introduction

1.1 Outline

In this thesis I will detail the fundamental principles of the strontium optical lattice clock (OLC) and explain why these features make it an extremely useful system not just for metrology, but for exploring open scientific questions from disparate areas of physics and, in particular, as a quantum simulator for exotic condensed matter systems. The principle considerations for modifying the existing OLC architecture in order to systematically study spin-orbit coupling and simulate the Fermi-Hubbard model of condensed matter physics will be described. I will discuss the motivation for confining atoms in tight periodic potentials for the purposes of metrology, the behaviour of such Fermions in periodic potentials and the methods involved in extremely precise spectroscopy of this behaviour. This will lead us to an understanding of how the 1D optical lattice is a useful analog to a number of real quantum systems and can be used to simulate the behaviour of such systems in a highly tunable way. Finally, I will describe the system I developed for intensity stabilising and dynamically ramping the incoming and retro reflected dipole beams which comprise the optical lattice, allowing us to vary the relevant experimental parameters to probe fermionic spin-orbit coupling in the lattice.

1.2 Building a good clock

There are three components to all clocks. They are: a periodic phenomenon, a counter, and a reference. The simplest clock is perhaps a sundial. The periodic phenomenon being the Earth rotating on its axis, causing the sun to arc across the sky and the shadow clock hand to trace a circular path around its *gnomon*. Each cycle represents a day and the circular path can be subdivided into hours. Similarly, we can count cycles of the Earth around the sun itself and label this a year.

In reality neither of these time bases is nearly good enough for modern life and so we have developed clocks whose periodic phenomenon is mechanical in nature and shorter timescale. The grandfather clock for example uses a pendulum, whose period is approximately given by $T = 2\pi\sqrt{L/g}$. The best mechanical oscillators are the quartz crystals found, among many

other places, in wrist watches. These are very high Q (quality factor) crystal oscillators[1] which are laser trimmed to resonate at a precise frequency. However, even these mechanical oscillators must be referenced to something. Initially these references remained astrological in nature; now the references are *even* better clocks and ultimately the atom.

A clock works by assigning some time T to a known number of cycles, n, at a known frequency f_c where

$$T = nt_c = n\frac{1}{f_c} \tag{1.1}$$

and we can find the uncertainty ΔT for variation Δf in the frequency and discover

$$\frac{\Delta T}{T} = -\frac{\Delta f}{f} \tag{1.2}$$

A "good" clock should minimise the error in T and so seeks to minimise $\Delta f/f$. The goal of the clock builder is therefore, crudely speaking, to decrease Δf while increasing f.[2]

1.3 Atoms as frequency standards

In the goal of searching for improved fractional uncertainty $\Delta f/f$ the move to atomic transitions is a natural one[3]. Atomic transitions are incredibly high frequency and can have staggeringly small linewidths. Additionally, atoms are the same everywhere. Unlike mechanical oscillators, where variations in design from one clock to the next cause separate clocks to run at different speeds, atoms of the same species are all pre-made ticking at an identical rate.[4]

[1] Although interestingly not as high Q as the Earth's rotation: the very best quartz oscillators have Q $\sim 10^7$ whereas the Earth, with short term length-of-day variations ~ 0.1 ms, has Q $\simeq 10^9$

[2] it is worth noting that real clocks are better analysed by their Allan Deviation which is a more appropriate measure of the stability of a clock over time, but the over simplified treatment captures enough of the behaviour for now.

[3] the utility of atoms as frequency standards was perhaps first noted by Lord Kelvin in 1879 [2] who noted: "*atoms* [such as] *hydrogen or sodium,* [are] *ready made in infinite numbers, all absolutely alike in every physical property. The time of vibration of a sodium particle corresponding to any one of its modes of vibration is known to be absolutely independent of its position in the universe, and it will probably remain the same so long as the particle itself exists*"

[4] albeit with a few important caveats: environmental effects perturb atomic energy levels and relativistic effects warp space-time, changing the 'ticking' of our clocks.

As mentioned, mechanical clocks, susceptible to variation in design/manufacture, have no intrinsic reference. Moreover, while on Earth we can all agree on celestial time standards, there may conceivably come a time when we need a time basis that extends beyond our own world!

An atomic time standard has long been established, with the SI second being redefined in 1967 as "*the duration of 9,192,631,770 periods of the radiation corresponding to the transition between the two hyperfine levels of the ground state of the caesium 133 atom*" [3]. The establishment and dissemination of a reliable and accurate frequency standard is vital for an incredible number of aspects of modern life from communication protocols in cellular networks and the internet, to satellite navigation (GPS runs by triangulating positions from the relative delay in the time signals broadcast by several satellites) and financial markets rely on being able to precisely synchronise trading.

Atomic clocks work by referencing an electromagnetic oscillator to a narrow atomic transition. This is shown for the case of the optical lattice clock below (figure 1.1). In the past atomic clocks such as the caesium fountain clocks have operated in the microwave domain where the stabilised clock frequency can be directly read out by electronics. In the terahertz domain this is much less straightforward. The advent of the optical frequency comb (discussed in more detail in section 2.5) allowed for counting in the microwave domain by using a heterodyne beat. The beat signal can inherit the stability afforded by optical clock frequencies while being read in the microwave domain, leading to an overall improvement in clock performance.

Optical atomic clocks can also be used to advance fundamental physics research. They have been used to precisely test the theory of relativity [4, 5] and it is hoped that future improvements will allow physicists to detect gravitational waves [6], design experiments to search for dark matter [7, 8] and to detect possible variations in the fundamental constants consistent with proposed extensions to the standard model [9, 10]. To that end driving down the uncertainty has required a shift away from microwave transitions (as in caesium fountain clocks) to the optical domain.

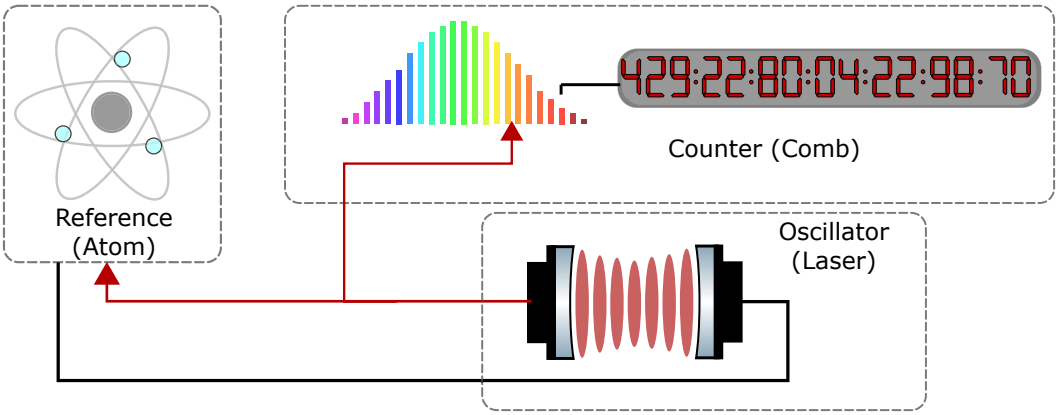

Figure 1.1: The components of the Optical Lattice Clock. An electromagnetic oscillator (optical reference cavity) is frequency locked to a well defined narrow electronic transition. The optical frequency of the oscillator can be mixed down to a microwave read out via a heterodyne beat with an optical frequency comb.

1.4 Quantum simulators

The idea of using one analogous quantum system to gain an insight into another, whose behaviour either cannot be easily experimentally probed or whose dynamics are too computationally intensive to directly calculate (in particular condensed matter systems) has been around for several decades. The idea, attributed to Feynmann [11], is seen as leading the way towards both quantum *computation* (as it is more typically thought of) where operations are performed on quantum-bits (qubits) to provide an exponential increase in computational speed versus a classical computer and to the quantum *simulation* of one quantum mechanical system with a physical analogue, as discussed in this thesis.

When we state that we wish to produce an analogous system, this really means that we wish to produce a physical implementation of an analogous Hamiltonian. One in which the parameters can be easily and controllably tuned and in which we can watch the state evolution dynamically. If we produce an analogous Hamiltonian, our solutions tell us something about how the 'real' system which we are studying behaves. By exploring the parameter space and behaviour of the model system we gain deeper understanding of the real system. Indeed we can make experiments and measurements which are impossible in the real system. As will be discussed later, one area of keen interest is probing the Fermi-Hubbard model of electrons in periodic potentials which, it is thought, can allow us to understand

high-temperature superconductivity [17, 18].

Optical lattices provide a very promising way to mimic the periodic potential experienced by electrons in crystalline solids, albeit with some crucial differences. In the optical lattice it is the atom moving in the potential of the light field which plays the role of the electron moving in the ion lattice. Importantly, atoms are i) vastly more massive than the electron ii) neutral. These are important differences. In the optical lattice atoms interact via dipolar effects, with much lower energies than the coulombic interactions of electrons in solids, requiring them to be cooled to ∼µK rather than ∼ 100 K temperatures. The physics also occurs on much larger length and timescales. Optical lattices have typical length scales of ∼ 1 µm rather than ∼ 0.1 nm for inter-atomic spacings and dynamics occur on µs to ms timescales rather than GHz – THz frequencies as one expects for the condensed matter system.

2 The Strontium Optical Lattice Clock

This section will give a brief overview of the strontium optical lattice clock in its current form. It is by no means exhaustive, and simply focuses on aspects which will be key to the main purposes of this report. The interested reader is directed to [12–16] for more experimental details.

2.1 Experiment overview

Shown below (figure (2.1)) is the layout of the Sr1 Optical Lattice Clock experiment. Two 40 L/s ion pumps are used to create a vacuum pressure in the science chamber of 10^{-11} Torr. Due to the relatively low vapour pressure of Sr, it is introduced to the chamber by means of an oven. Heated strontium atoms are emitted and roughly collimated by flanges at the output of the oven. The result is a hot thermal distribution of atoms in the direction of the science chamber.

To improve the loading efficiency of the 3D MOT in the science chamber, two additional techniques are employed the manipulate the velocity distribution. Firstly, transverse cooling is applied by means of perpendicular optical molasses beams, Doppler cooling motion perpendicular to the desired path. Secondly, atoms are axially cooled by means of a Zeeman Slower (ZS) as they approach the chamber. A strong magnetic field is created by a coil with increasing number of wound turns. As the atomic temperature is cooled, and the average velocity in the direction of the science chamber is decreased, the increased magnetic field shifts the resonance appropriately, balancing the Zeeman and Doppler shifts to maintain the detuning from resonance and therefore efficiency of the slowing beam. The profile of the wound coil is designed to maximise this process and the loading of the MOT.

The science chamber allows optical access for the two stages of 3D magneto optical trap. The red and blue MOT beams are overlapped at dichroic mirrors shown. To minimise tunnelling during clock operation a vertical lattice is used, creating a staggered potential $\Delta U = -mg\Delta z$ from site to site where Δz is the vertical offset between sites. The lattice enters the chamber at $\sim$19° from the vertical. The clock beam and lattice beam are overlapped at the lattice retro mirror ensuring that their wave vectors are parallel and have

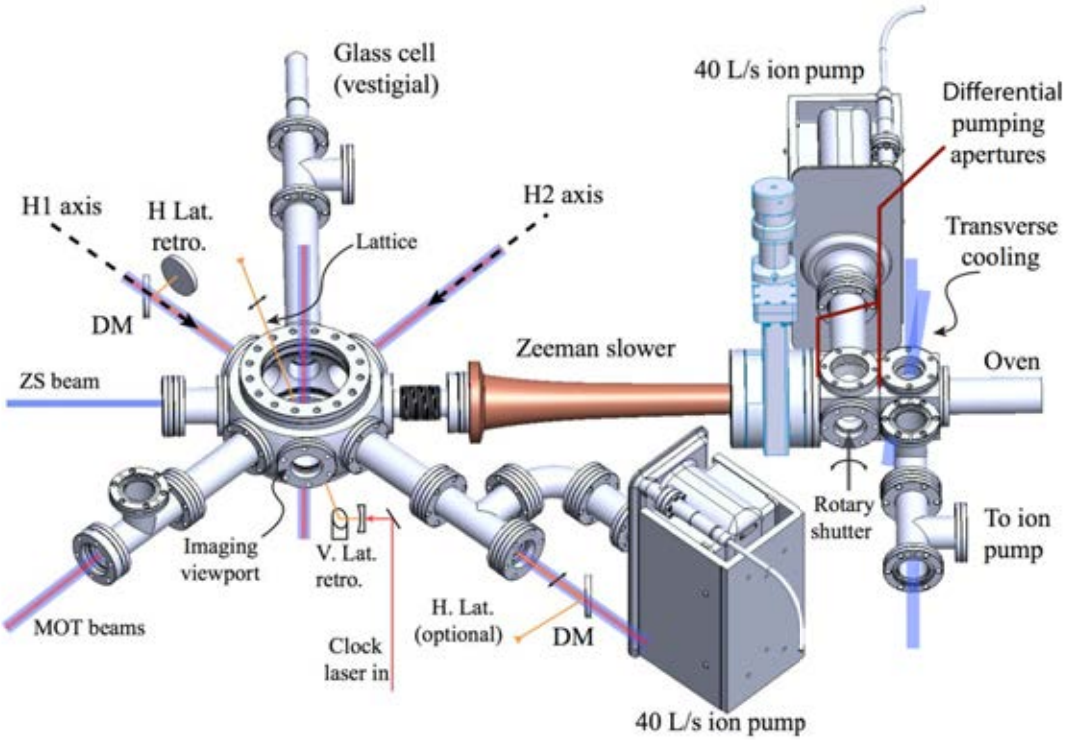

Figure 2.1: Schematic of science chamber for Strontium Optical Lattice Clock experiment (described in text).

correct relative polarization. The retro mirror also acts as a plane of reference from which vibration is common mode for both lattice and clock beams. Environmental noise in the clock path between the master laser and the final mirror is cancelled by means of fiber phase noise cancellation [19, 20]. By referencing both beams to the same final mirror it can be ensured that any uncancelled noise will not be differential which would introduce vibration noise into the atom readout.

State population readout, which will be discussed in more detail in section (2.6) is achieved via fluorescence counting using a photomultiplier tube (PMT).

2.2 Two-stage Magneto Optical Trap

Historically alkali atoms have formed the basis of cold atom experiments. Their single unpaired electron leads to a relatively simple electronic structure and their cooling transitions fall into convenient wavelengths for commercially available diode lasers. Strontium, on the other hand, is an alkaline-earth atom with two outer shell electrons leading to a richer elec-

tronic structure and an $\vec{S} = 0$ groundstate.

In strontium, the ^3P_J manifold offers interesting narrow features known as intercombination lines. These arise because the two electron singlet and triplet states in these alkaline-earth atoms are not pure LS states. This mixing causes a finite lifetime for these states and allows so-called 'forbidden', electric dipole transitions to the $^1S_0$ groundstate. The cycling $^1S_0 \rightarrow {}^3P_1$ transition can be used to cool and trap atoms in a magneto optical trap.

The narrowness of this line is both a difficulty and a blessing for strontium. The linewidth leads to an incredibly small velocity capture range (v_c=5.0 cm/s) with Γ=7.4 kHz, which requires that atoms be initially cold before loading the magneto-optical trap (MOT) so that a reasonable fraction of atoms can be trapped, since the capture range represents a larger proportion of all atoms at lower temperatures. However, the transition also allows very low final atom cloud temperatures without evaporation exactly because of its narrowness. The Doppler limited temperature (where the thermal velocity distribution width equates to a Doppler shift distribution equivalent to Γ) is given by

$$k_B T_D = \frac{\hbar\Gamma}{2} \tag{2.1}$$

For the $^1S_0$ to $^3P_1$ transition this equates to a T_D=180 nK. Indeed the transition is so narrow that in reality cooling becomes limited by the single photon recoil temperature $k_B T_R = \hbar^2 k^2/M$ limiting final temperatures in the MOT to approximately 1 μK [21].

In order to efficiently load such a narrow linewidth MOT, the atoms are first cooled on the strong $^1S_0$ to $^1P_1$ with Γ=30.5 MHz and T_D=720 μK. The pre-cooled cloud can then be loaded into the second stage MOT as described above. To maximise the efficiency of this transfer the narrow linewidth red MOT beams are modulated by means of a double passed AOM to broaden their effective linewidth to 1 MHz. This increases the phase space overlap between blue and red MOTs. The cloud is then compressed by increasing the field gradient and the modulation is removed leaving a single laser frequency. Atoms in the single frequency MOT can then reach their final temperature of $\sim$ 1 μK.

2.3 Recoil free spectroscopy

Even at the 1 μK level made possible by utilising the two stage magneto optical trap and the benefits of the alkali-earth electronic structure, the motion of the atoms, in particular the momentum kick associated with absorbing/emitting photons would greatly limit clock accuracy. Therefore the atoms are loaded into a deep optical lattice. The optical lattice will be discussed in greater detail in later chapters but the principle is that atoms confined to the wells of a deep optical lattice can enter the Lamb-Dicke regime [22, 23]. The atom's motion in the groundstate of the potential well is characterised by the extent of the wavefunction in the trap z_0. For the pseudo-harmonic lattice potential

$$z_0 = \left(\langle 0|\hat{z}^2|0\rangle\right)^{1/2} \approx \sqrt{\frac{\hbar}{2m\omega_z}}$$

is far smaller in extent than the wavelength of the light it interacts with. In such a situation the Lamb-Dicke parameter

$$\eta = k_c z_0 \ll 1$$

and the momentum of the atom is strongly decoupled from its internal state. This allows the bare transition to be probed without introducing frequency shifts from the momentum gained in absorbing/emitting clock photons, allowing the narrowness of the $^1S_0$ to $^3P_0$ state to be truly exploited as a metrological tool and frequency standard.

2.4 Ultra-stable laser

In order to make use of the incredibly narrow mHz linewidth of the clock transition it is vital that a suitably narrow probe laser is used. Indeed, as described above, the laser itself *is* the clock. The success of previous clock experiments at JILA at utilising the extraordinarily narrow $^1S_0$ to $^3P_0$ clock transition for metrology is due in no small part to the successful implementation of an ultra-stable clock laser whose performance allows us to take better advantage of these narrow spectral features.

The light source for both the Sr optical clocks at JILA is 698 nm external cavity laser diode frequency stabilised via the Pound-Drever-Hall technique to a 40 cm reference cavity constructed from a ULE (Ultra Low Expansion) glass spacer (figure 2.2). It has been shown to reach 1.6×10^{-16} fractional uncertainty between 1 and 1000s, the thermal noise floor of the cavity. By analysing the power spectral density of the cavity noise an effective linewidth of

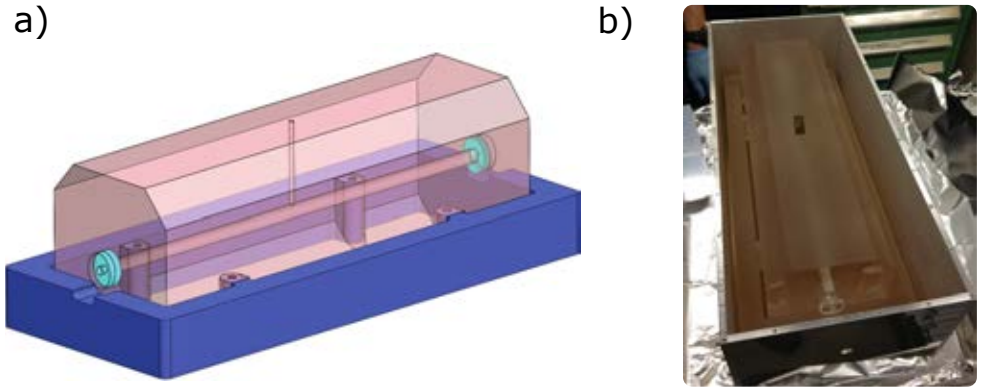

Figure 2.2: The 40 cm ULE clock reference cavity. a) a CAD drawing of the cavity used for stress simulations b) the cavity installed in first layer vacuum enclosure.

26 mHz [24] has been calculated. The precise details of the ultra-stable laser used in the strontium experiments have been detailed extensively elsewhere [15].

The ideas expressed in this work will concern the use of the precise spectroscopic capabilities afforded by the optical clock not for timekeeping but for understanding the behaviour of atoms in the environment of the optical lattice. The clock laser precision offers a novel way to see such behaviour in very high definition.

2.5 Frequency combs

The advent of the octave spanning optical frequency comb allowed optical clocks to become a reality [25]. The frequency comb generates optical pulses at repetition rate τ (where generally $\tau \sim$ femtoseconds). In the frequency domain this generates a spectrum of narrow comb teeth given by

$$\nu_n = n f_{rep} + f_0 \tag{2.2}$$

where $f_{rep} = 1/\tau$ and f_0 is an underlying optical frequency which describes the phase difference between pulses. The comb spectrum covers at least an octave ($f_2 = 2 \times f_1$) and can be used to compare the phase of two different lasers over 100s of THz. Both f_{rep} and f_0 can be stabilised to a local oscillator (for example the clock laser) and inherit the stability, meaning that optical frequency readout is possible without degradation of the

clock's stability [26].

2.6 State counting

The Strontium clock uses direct counting of atomic state populations to make spectroscopic measurements both when operating as a clock or currently as a simulator for solid state physics. When operating as a clock, the laser is alternately detuned $\pm\Delta$ from the atomic transition peak such that it sits on either side of the Rabi lineshape and a π-pulse excites an excited state $f_{\pm} = N_e/(N_g + N_e)$. From the difference in excited state fraction either side of the peak, and knowledge of the lineshape, the location of the resonance can be inferred in two measurements. This is then fed back to steer the local oscillator.

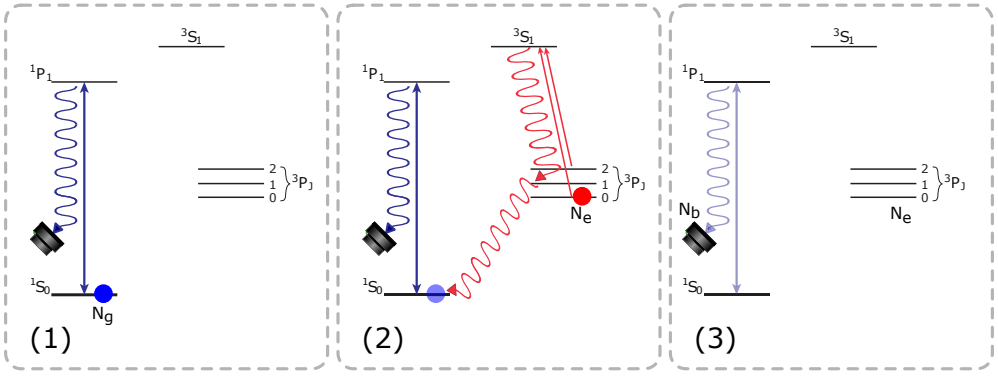

Figure 2.3: State Counting. Both the ground and excited state populations are counted using fluorescence on the $^1S_0 \rightarrow {}^1P_1$ transition. (1) Groundstate population is counted. (2) Excited state atoms are optically pumped into the groundstate via the $^3S_1$ level and counted via $^1P_1$ fluorescence. (3) A background photon count is made.

The procedure for state counting is shown in figure 2.3. First the groundstate population is measured using the strong $^1S_0 \rightarrow {}^1P_1$ transition. A photomultiplier tube (PMT) is used to count the atom number which is proportional to photon counts. After 5 ms all groundstate atoms have been heated out of the trap by the scattering process. Next, the excited state atoms are optically pumped into the $^1S_0$ groundstate using a broad π-pulse. The counting process is then repeated using the blue transition and the PMT counts reveal the excited state population. After another 5 ms pulse all excited state atoms have been heated out of the trap and a third 5 ms pulse is used to count the background photon count. These three

measurements enable the excited state population fraction and uncertainty to be measured each experimental cycle.

3 Optical Lattices

3.1 Neutral atom traps

Unlike ions, which lend themselves to being readily trapped in a confining potential due to their strong coulomb interaction[5], creating strong, conservative potentials with neutral atoms is less straight forward. In the ion trap, the coulomb interaction is so strong that trap frequencies of $\sim$ MHz or higher and depths of several eV can be readily achieved. This allows ion trap systems to reach well into the Lamb-Dicke regime where, for example, entanglement and sideband cooling can be experimentally achieved [27, 28].

For neutral atoms, the dipole force can be utilised to create a spatially confining potential giving neutral atom physicists a similar tool to the ion trappers [29]. The dipole trap utilises the induced dipole moment of atoms in the presence of a strong field due to the AC Stark effect to create a spatially conservative potential. The advent of high powered lasers with the required coherence has led to far-off-resonant dipole traps becoming common place in the cold atom community.

As will be seen, dipole traps tend to be far from resonances as this maximises the confinement from the dipole effect while reducing the undesired effects of radiation pressure from scattering. For typical laser powers, a far off resonant dipole trap might have a depth of order mK and so is usually loaded from a cold atom sample prepared via a magneto-optical trap. Further cooling is possible within the trap, for example, via evaporation.

The utility of the dipole force in creating novel trap geometries is also a large benefit. Optical lattices, so-called crystals of light, are created by counter-propagating beams in one or more dimensions. The interference of the beams leads to a standing wave formation where atoms can be trapped at the high (or low) intensity regions in the case of a red (blue) detuned laser. More complex lattice geometries can be realised by changing relative beam angles, adding multiple wavelengths or by introducing frequency doubled or tripled laser beams to

[5]It should be noted that Earnshaw's theorem disallows charges being trapped in static electro-magnetic fields and thus all ion traps are comprised of one or more oscillatory fields

synthesize a desired trap structure. Additionally one can easily create confining potentials which are anisotropic or mimic so-called toy models of physics such as the double well or box potential.

3.2 Optical dipole traps

3.2.1 The dipole force

The dipole force arises from the dispersive interaction between the induced dipole moment with the intensity gradient of the light field. We begin by describing the electric field $\vec{E}(t)$ of our laser and the dipole $\vec{p}(t)$ which oscillates in sympathy with the driving field.

$$\vec{E}(\mathbf{r},t) = \hat{e}\tilde{E}(\mathbf{r})\exp(-i\omega t) + c.c. \tag{3.1}$$

$$\vec{p}(\mathbf{r},t) = \hat{e}\tilde{p}(\mathbf{r})\exp(-i\omega t) + c.c. \tag{3.2}$$

where $\tilde{p} = \alpha(\omega)\tilde{E}$, and $\alpha(\omega)$ is the polarizability. The interaction potential can be written as

$$U_{dip}(\mathbf{r}) = -\frac{1}{2}\langle \mathbf{pE} \rangle = -\frac{1}{2\epsilon_0 c}\,\mathrm{Re}(\alpha) I(\mathbf{r}) \tag{3.3}$$

The factor $1/2$ comes from the fact that the dipole is induced[6]. From the expression for the dipole potential we can derive the confining dipole force as

$$F_{dip}(\mathbf{r}) = -\nabla U_{dip}(\mathbf{r}) = \frac{1}{2\epsilon_0 c}\,\mathrm{Re}(\alpha)\nabla I(\mathbf{r}) \tag{3.4}$$

Clearly in the case of a Gaussian beam this is a restoring force both radially and axially towards the focus. We can also use the approach of the classical dipole to consider the scattering rate. First, the power absorbed by the atom and re-emitted as dipole radiation is given by

$$P_{abs} = \langle \mathbf{E} \rangle = 2\omega\,\mathrm{Im}(\tilde{p}\tilde{E}^*) = \frac{\omega}{\epsilon_0 c}\,\mathrm{Im}(\alpha) I(\mathbf{r}) \tag{3.5}$$

and by dividing by the energy per photon we arrive at a scattering rate

$$\Gamma_{sc} = \frac{P_{abs}}{\hbar\omega} = \frac{1}{\hbar\epsilon_0 c}\,\mathrm{Im}(\alpha) I(\mathbf{r}) \tag{3.6}$$

[6] see Virial Theorem

By treating the induced dipole of the atom as a simple oscillator in this way, we have derived expressions for both the confining potential and the scattering rate in the trap in terms of the polarizability $\alpha(\omega)$. This simple approach is perfectly valid for neutral atoms and captures the physics for traps both on resonance and for far-detuned fields.

In general, calculation of the polarizability $\alpha(\omega)$ of many level atoms with complex electronic structures requires a full quantum mechanical calculation. An intuitive picture can, however, be gained by treating the polarizability classically as in the Lorentz model. While not entirely accurate (certainly near resonance and for strong fields where saturation effects are relevant) this will be sufficient to develop an intuition for some of the considerations when trapping neutral atoms.

3.2.2 Polarizability

In the Lorentz model, the electron is bound to the atom elastically, with eigenfrequency ω_0, the transition frequency. The polarizability is calculated by considering the dipole moment $\tilde{p}(t) = -e\tilde{x}(t)$ along with $p(t) = \alpha(\omega)E(t)$. The electron position is calculated by solving the classical equations of motion:

$$\ddot{x} + \Gamma_\omega \dot{x} + {\omega_0}^2 = -\frac{eE(t)}{m_e} \tag{3.7}$$

where $\Gamma_\omega = e^2\omega^2/6\pi\epsilon_0 m_e c^3$ is the damping rate due to radiative losses [30]. Solving equation (3.7) for the oscillating electric field $E(t)$ in equation (3.1) yields an expression for the polarizability

$$\alpha(\omega) = \frac{e^2}{m_e}\frac{1}{{\omega_0}^2 - \omega^2 - i\omega\Gamma_\omega} \tag{3.8}$$

which can be written in terms of the 'on-resonance' damping $\Gamma = (\omega_0/\omega)^2\Gamma_\omega$ to give the expression

$$\alpha = 6\pi\epsilon_0 c^3 \frac{\Gamma/{\omega_0}^2}{{\omega_0}^2 - \omega^2 - i(\omega^3/{\omega_0}^2)\Gamma} \tag{3.9}$$

in which the explicit use of Γ draws obvious connections with the quantum mechanical linewidth for the transition. Indeed, one can replace Γ with a quantity calculated using the

dipole matrix element for the transition to find a more accurate semi-classical approximation of α.

A full discussion of accurately calculating the polarizability for a many level atom is beyond the intended scope of this thesis. For ^{87}Sr the calculation is detailed elsewhere (e.g. [15]) in the context of predicting the so-called 'magic' wavelength. This is the wavelength at which the AC Stark shift is equal in both the ground and excited clock state so that the effect of the confining potential does not shift the bare clock transition frequency used for metrology [31].

3.2.3 Dipole potential and scattering in rotating wave approximation

In the case of far off resonant light, we can use equation (3.9) for $\alpha(\omega)$ to rewrite our earlier expressions (equation (3.3) and (3.6)) for the dipole potential and scattering rate in terms of Γ as

$$U_{dip}(\mathbf{r}) = \frac{3\pi c^2}{2{\omega_0}^3}\left(\frac{\Gamma}{\omega_0 - \omega} + \frac{\Gamma}{\omega_0 + \omega}\right) I(\mathbf{r}) \approx \frac{3\pi c^2}{2{\omega_0}^3}\left(\frac{\Gamma}{\Delta}\right) I(\mathbf{r}) \tag{3.10}$$

and

$$\Gamma_{sc}(\mathbf{r}) = \frac{3\pi c^2}{2\hbar{\omega_0}^3}\left(\frac{\omega}{\omega_0}\right)^3 \left(\frac{\Gamma}{\omega_0 - \omega} + \frac{\Gamma}{\omega_0 + \omega}\right)^2 I(\mathbf{r}) \approx \frac{3\pi c^2}{2\hbar\omega^3}\left(\frac{\Gamma}{\Delta}\right)^2 I(\mathbf{r}) \tag{3.11}$$

In the second expression we use the rotating wave approximation and lose the counter rotating term. This is a reasonable approximation when the driving field is of order ω_0. We also introduce the detuning $\Delta = \omega_0 - \omega$ to simplify the notation. It is worth noting that for a simple two level system this expression already captures the difference in behaviour for atoms trapped in 'blue-detuned' ($\Delta < 0$) and 'red-detuned' ($\Delta > 0$) traps, in that for 'red-detuned' traps the potential is conservative in regions of high intensity, whereas for 'blue-detuned' traps it is conservative in regions of low intensity. Although this work will detail exclusively 'red-detuned' traps it is worth stating that atoms can be held in the intensity minima of 'blue-detuned traps in some 3D geometries.

The trapping potential goes as $1/\Delta$, but the scattering rate in the trap goes as $1/\Delta^2$, therefore, since it is nearly always important to minimise scattering vs. confinement in the trap, typically Δ is chosen to be as large as practically possible. For ^{87}Sr the magic

wavelength criteria leads to choosing a confining wavelength in the near infra-red at $\simeq 813.4$ nm. At present this constraint on Δ has no practical bearing on the experiment, although it is thought that Raman scattering from the lattice beams which couples $^3P_0$ to the other levels in ^3P_J manifold via the $^3S_1$ state will ultimately limit the clock state lifetime and therefore presents a challenge to clock stability at the $\sim 10^{-19}$ level. The Raman scattering rate from the $^3P_0$ state is a matter of ongoing investigation.

3.2.4 Magic wavelength traps

In an atomic clock the transition frequency is used as an unambiguous reference and should have a definite frequency. Unfortunately, the confining action of the dipole force also causes a differential stark shift in the $|g\rangle$ and $|e\rangle$ states given by

$$\Delta\nu_c = -\frac{1}{2\epsilon_0 c}\Delta\alpha(\omega_L)I(z,r) \tag{3.12}$$

where $\Delta\alpha(\omega_L)$ is the difference in polarizability of the two states in the lattice. In order to define the clock frequency non-arbitrarily, it is vital that it be operated at one of the so-called 'magic' wavelengths. At such wavelengths the polarizability is the same in both the ground ($^1S_0$) and excited ($^3P_0$) states. This means that the transition frequency is the same as the bare transition frequency in an unconfined atom. As stated the strontium optical lattice clock operates at approximately 813.4 nm where there is a shallow zero crossing in $\Delta\alpha(\omega_L)$.

3.3 Periodic Potentials

3.3.1 One dimensional optical lattice

An optical lattice is produced by the interference pattern of two superimposed beams which cause a standing wave of high and low intensity regions. The dipole force confines atoms in the antinodes of the intensity pattern. Typically the original beam is retro reflected such that the interference is coherent and lattice sites are fixed in space. This also has the advantage that vibration in the optical path is common mode for both beams other than on the retro mirror itself. For a single Gaussian beam close to the focus (i.e. $z \ll z_r$ and $R(z) \to \infty$) we can write the electric field as

$$E_{\rightarrow}(r,z) = E_0 \frac{w_0}{w(z)} \exp\left(\frac{-r^2}{w(z)^2}\right) \exp\Big(-ikz\Big) \tag{3.13}$$

where $w(z) = w_0\sqrt{1+(z/z_r)^2}$ is the beam waist, w_0 is the waist at the focus, z_r is the Raleigh range and k is the wavenumber. The time dependence $e^{i\omega t}$ is omitted for brevity as the oscillation is too fast to drive the atoms' position. We have similarly ignored the small change in phase associated with displacement from the centre of the beam (Guoy Phase) since we assume we are exceptionally close to the beam focus. The retro reflected beam is calculated trivially by changing the directionality $k \rightarrow -k$. The final intensity can then be calculated by

$$I(r,z) = |E_{\rightarrow}(r,t) + E_{\leftarrow}(r,t)|^2 \tag{3.14}$$

where, in general, the electric field strength of the retro reflected by is modified by some constant $\sqrt{f}$ where $0 < f \leq 1$ by the reflection process. Using this expression for intensity we can write the potential within the trap in the form of equation (3.3) where we have converted to units of power rather than intensity since this is experimentally accessible parameter. (Note: $P_2 = fP_1$ where P_1 and P_2 are the ingoing and retro reflected beam powers respectively.)

$$V(r,z) = -\Big(V_{const} + U_z \cos^2(kz)\Big) e^{-2r^2/{w_0}^2} \tag{3.15}$$

where

$$V_{const} = \frac{\alpha(\omega)}{\pi\epsilon_0 c {w_0}^2}\big(P_1 + P_2 - 2\sqrt{P_1 P_2}\big)$$

and

$$U_z = \frac{4\alpha(\omega)}{\pi\epsilon_0 c {w_0}^2}\sqrt{P_1 P_2}$$

We will return to equation (3.15) when we consider controlling the transition from strong to weak periodic confinement. It is often convenient to write the trap potential U_z in terms of the recoil energy of a single lattice photon $E_r = \frac{\hbar^2 {k_L}^2}{2m}$. When the lattice depth is more than a few E_r and the temperature is suitably cold so that atoms primarily occupy the lowest motional bands of the trap, we can use $\cos^2(kz) \simeq 1 - k^2 z^2$ to approximate each site of the lattice by a parabolic potential centred at $z = z_0 + n\frac{\pi}{k_L}$, the position of the n^{th} lattice site. One can then write the trap frequency ν_z as

$$\nu_z \approx \frac{E_r}{\pi\hbar}\sqrt{\frac{U_z}{E_r}} \tag{3.16}$$

In this work we will refer to both E_r and ν_z as appropriate.

3.3.2 Band structure

We now consider the eigenstates of atoms in our periodic potential. In general, particles confined in periodic potentials are described in the Bloch basis. Bloch's Theorem tells us that the eigenstates of a periodic potential take the form

$$\phi_q^{(n)}(x) = e^{iqx/\hbar}u_q^{(n)}(x) \tag{3.17}$$

They are composed of a continuous wave-like function characterised by q, the quasimomentum, multiplied by the Bloch function $u_q^{(n)}(x)$ which has the same periodicity as the underlying potential. The notation here implies $q \in \{BZ\}$ and n denotes the energy band since multiple eigenenergies exist for a single Bloch function. The eigenfunctions satisfy

$$\hat{H}\phi_q^{(n)}(x) = E_q^{(n)}\phi_q^{(n)}(x) \tag{3.18}$$

where $\hat{H} = \frac{1}{2m}\hat{p}^2 + V(x)$ and $V(x)$ is the periodic potential in the system (for the case of the 1D optical lattice this is derived in equation (3.15)). The Bloch states i) are delocalised in space ii) form a complete orthogonal basis.

Using Bloch's theorem, we can rewrite our Hamiltonian replacing the eigenfunctions $\phi_q(x)$ with the Bloch functions $u_q(x)$ as

$$H_B u_q^{(n)}(x) = E_q^{(n)}u_q^{(n)}(x) \tag{3.19}$$

where $H_B = \frac{1}{2m}(\hat{p}+q)^2 + V(x)$. Since both our Bloch functions and our underlying potential share the same periodicity we proceed by expanding both as discrete Fourier sums

$$V(x) = \sum_r V_r e^{i2rkx} \qquad \text{and} \qquad u_q^{(n)}(x) = \sum_l c_l^{(n,q)} e^{i2rkx} \tag{3.20}$$

Using these series expansions we can rewrite the potential and kinetic energy terms in our Hamiltonian as

$$V(x)u_q^{(n)}(x) = \sum_l \sum_r V_r e^{i2(r+l)kx} c_l^{(n,q)} \tag{3.21}$$

and

$$\frac{(\hat{p}+q)^2}{2m} u_q^{(n)}(x) = \sum_l \frac{(2\hbar k l)^2}{2m} c_l^{(n,q)} e^{i2rkx} \tag{3.22}$$

Since our atoms exist very close to the focus ($z \ll z_r$) of our optical lattice, we can ignore the small variation of the confining beams in the region of the trap due to the narrowing of the laser beams. Additionally, when calculating the eigenstates of the periodic potential we can ignore any constant terms and so simply write

$$V(x) = -U_z \cos^2(kz) = -\frac{U_z}{4}\left(e^{2ikx} + e^{-2ikx} + 2\right) \tag{3.23}$$

We then identify that in the series expansion of the potential in equation (3.20) the only non-vanishing terms are $r = 0, -1, 1$, where $V_{-1} = V_1 = -U_z/4$ and $V_0 = -U_z/2$. Since terms in V_0 are constant we can remove them from the calculation and simply expand over $r \in \{-1, 1\}$.

The series approximation for the Bloch function $u_q^{(n)}(x)$ is harder to constrain. Clearly as $l \to \pm\infty$ we converge on the analytic solution. However, in practise calculations with large l are computationally intensive and typically unnecessary. When calculating the eigenenergies here we use $-10 \leq l \leq 10$ which does a very good job of capturing the shape of the first few energy bands.

It is also worth noting at this stage that when we consider the band structure in the axial direction we are implicitly assuming that all atoms reside at $r = 0$. This is an even stronger statement than that the radial temperature is zero, since even in the lowest radial band the atomic wavefunction has some radial extent. In reality, there is a small correction in the axial part of the atom wavefunctions which comes from the Gaussian confinement in the radial direction. As the atom wavefunction spreads out radially it explores a weaker

axial potential than that described by $V(x, r = 0) = -U_z \cos^2(kz)$. The correction is small, and the approach detailed above does a good job when calculating the eigenenergies of the lattice. Discussion of axial radial coupling terms can be found in [32]

We can now calculate the eigenstates and eigenenergies of our system by rewriting equation (3.19) in matrix form in terms of our series expansion.

$$\sum_l H_{l,l'} c_l^{(n,q)} = E_q^{(n)} c_l^{(n,q)} \qquad \text{where} \qquad H_{l,l'} = \begin{cases} (2l + q/\hbar k)^2 & l = l' \\ -V_0/4 & |l - l'| = 1 \\ 0 & \text{else} \end{cases} \tag{3.24}$$

This tri-diagonal matrix may be solved for the eigenvectors $c_l^{(n,q)}$ and eigenenergies $E_q^{(n)}$ in terms of quasimomentum q. The eigenenergy spectrum is known as the band structure. The first few bands are shown (figure (3.1)) for a variety of trapping potentials U_z. An intuitive picture can be achieved by considering the band structure as slowly progressing from the free particle dispersion relation at $V_0 = 0\ E_r$ to flat harmonic oscillator levels as the periodic potential is slowly ramped up. For a suitably deep lattice it is common to approximate the sinusoidal element of the potential with a harmonic term centred around each lattice site. We also see that as the depth of the corrugation is increased, the energy gap between bands increases.

3.3.3 Wannier functions

The Bloch states $\phi_q^{(n)}(x)$ are entirely delocalised across all sites in the lattice. They have definite quasimomentum q but no definite position. A complementary set of wavefunctions can be constructed where particles are constrained to a single site but with no definite quasimomentum. These are the Wannier functions [33]. The Wannier function for a particle at position x_i (being the centre of the ith lattice site) is given by the discrete Fourier transform of the Bloch states:

$$w_n(x - x_i) = \frac{1}{\sqrt{L}} \sum_{q \in \{BZ\}} e^{-iqx_i/\hbar} \phi_q^{(n)}(x) \tag{3.25}$$

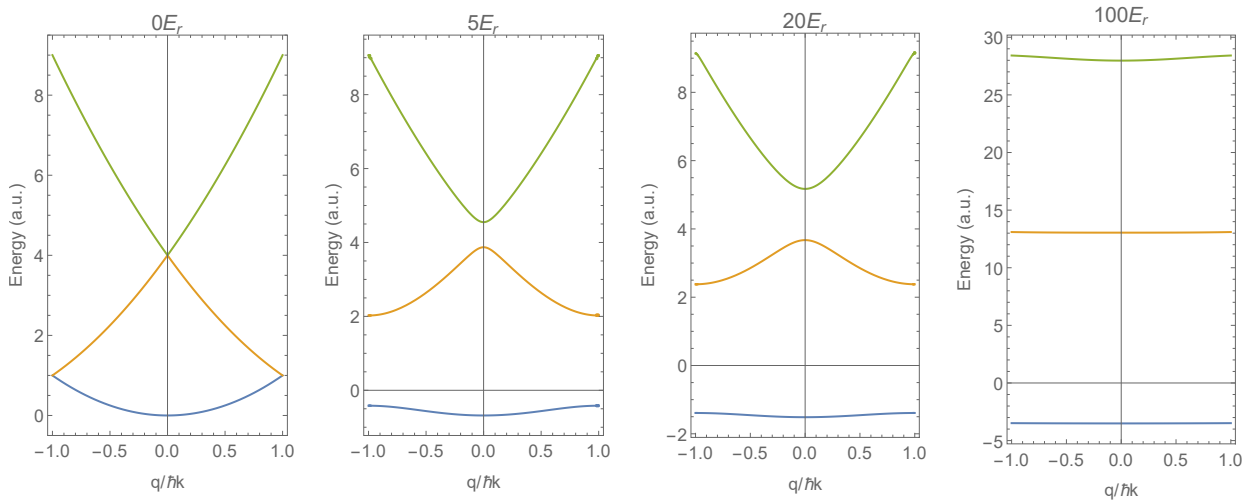

Figure 3.1: Bloch bands calculated for trapping potentials of 0 E_r, 5 E_r, 20 E_r and 100 E_r. The bands show the progression from a free particle dispersion relation at 0 E_r to something which approximates harmonic oscillator levels as $V_0 \to \infty$

3.3.4 Tunnelling in the optical lattice

The Bloch bands can be used to directly calculate the tunnelling matrix element J_n for a particular band, which is given by

$$J_n = \frac{1}{4}\left(\max\left(E_q^{(n)}\right) - \min\left(E_q^{(n)}\right)\right) \tag{3.26}$$

The tunnelling rate falls exponentially with increasing lattice depth and tends towards the free particle kinetic energy at $V_0 = 0$.

The tunnelling rate in the lattice is calculated for the first two Bloch bands (figure 3.2). The tunnelling rate is much larger in the second motional band, consistent with the reduced Brillouin zone picture shown in section 3.3.2. In section 5.3 we discuss how we can prepare atoms in different motional bands as a novel way to tune the tunnelling parameter J.

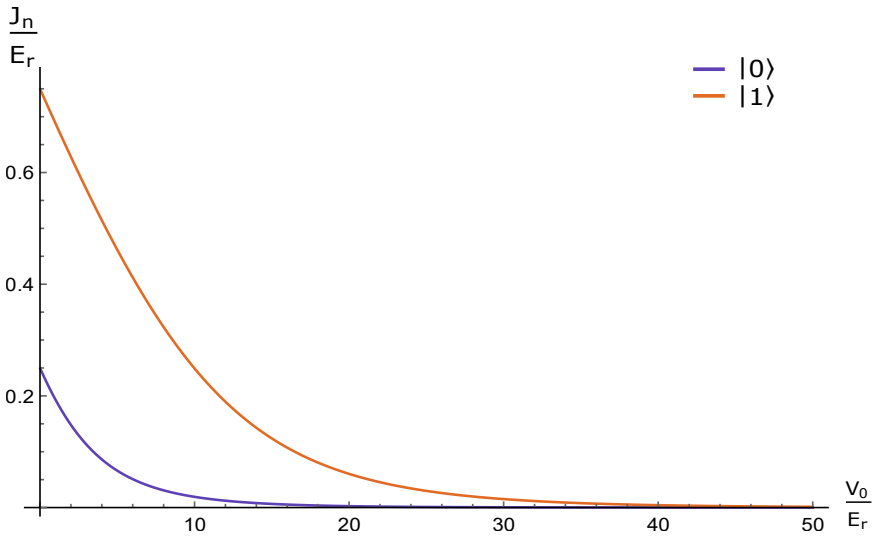

Figure 3.2: Tunnelling rate in the two lowest Bloch bands, $|0\rangle$ and $|1\rangle$ as a function of trap depth V_0. At $V_0 \to 0$ the tunnel rate is equal to the free particle kinetic energy at the BZ edge.

3.4 Clock transitions in a deep lattice

In the Lamb-Dicke regime (see Section 2.3) the atoms motion and its internal state are strongly decoupled. In the case where ω_z is greater than the width of the motional band, transitions $|g, m\rangle \to |e, m\rangle$ and $|g, m\rangle \to |e, m+1\rangle$ can be spectroscopically resolved. As shown in figure 3.1, for a suitably deep lattice the potential is pseudo-harmonic and the energy bands become flat. Figure 3.3 shows spectroscopy of the clock state for a deep ($U_z = 30.5\ E_r$) lattice. We see three distinct sidebands in addition to the narrow clock transition.

The 'red' sideband at negative detuning corresponds to transitions from the $n_z = 1$ to $n_z = 0$ bands. This is strongly suppressed for a 1 μK atom temperature where the vast majority of atoms reside in the motional groundstate of the trap. Two 'blue' sidebands are seen corresponding to transitions which promote the atom to the $n_z = 1, 2$ motional bands.

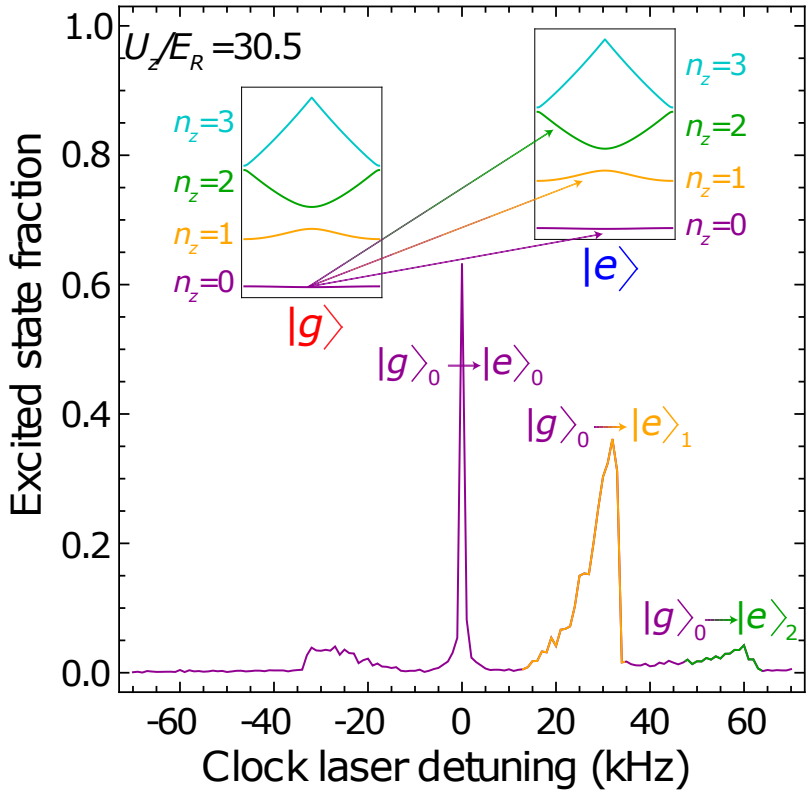

Figure 3.3: Rabi spectroscopy of the clock transition in a deep lattice (30.5 E_r). Transitions between different motional bands can be resolved as distinct sidebands. The width of the $|g\rangle_0 \rightarrow |e\rangle_1$ sideband stems from anharmonicity in the trap.

4 Intensity Stabilisation and Dynamic Control

In order to use the strontium OLC as a quantum simulator we needed to add the capability to intensity stabilise and dynamically ramp the incoming and retro reflected dipole beams which comprise the optical lattice in a low noise and high fidelity way. The scheme I developed increases the capabilities of the optical lattice especially in regard to its use as a quantum simulator and has made possible the foray into the world of spin-orbit coupling with interactions described in this thesis. This section discusses the design of the intensity servo, the relevance of the intensity noise spectrum on atoms in the lattice and the considerations for improving servo characteristics.

4.1 Lattice laser system

4.1.1 Dipole beam

As discussed, the magic wavelength optical lattice operates in the near infrared at ∼813.4 nm. In previous generations of the 'Sr1' OLC the light source for the optical lattice had been an ∼100 mW NIR laser diode slaved to a master ECDL operating at the magic wavelength. A final power of 300 mW was achieved by seeding a tapered amplifier with specially designed filters to remove amplified spontaneous emission. The new experiments were fortunate to make use of an MSquared Ti:Sapph laser (SolsTiS) which provides up to 5 W of coherent 813 nm light. The SolsTiS is pumped with an 18 W seed laser from Lighthouse Photonics (Sprout).

Figure (4.1) shows the optical set up for the in going lattice laser. The Ti:Sapph passes through a -30 dB optical isolator. The rejection port of this isolator can be used to monitor retro reflected light which has passed back through the high power fiber. Various $\lambda/2$ wave-plates and beamsplitter pairs separate small fractions of the beam for purposes of power monitoring, optional frequency locking (to either a spectrum analyser or via a heterodyne beat with the frequency comb) or to distribute power to the other strontium optical clock 'Sr2'. A 30 MHz AOM is used for intensity stabilisation. The m=1 order beam passes through a 1:2 telescope and is fiber coupled to the experiment. A small portion of the 0^{th} order beam is used for monitoring and the rest is dumped.

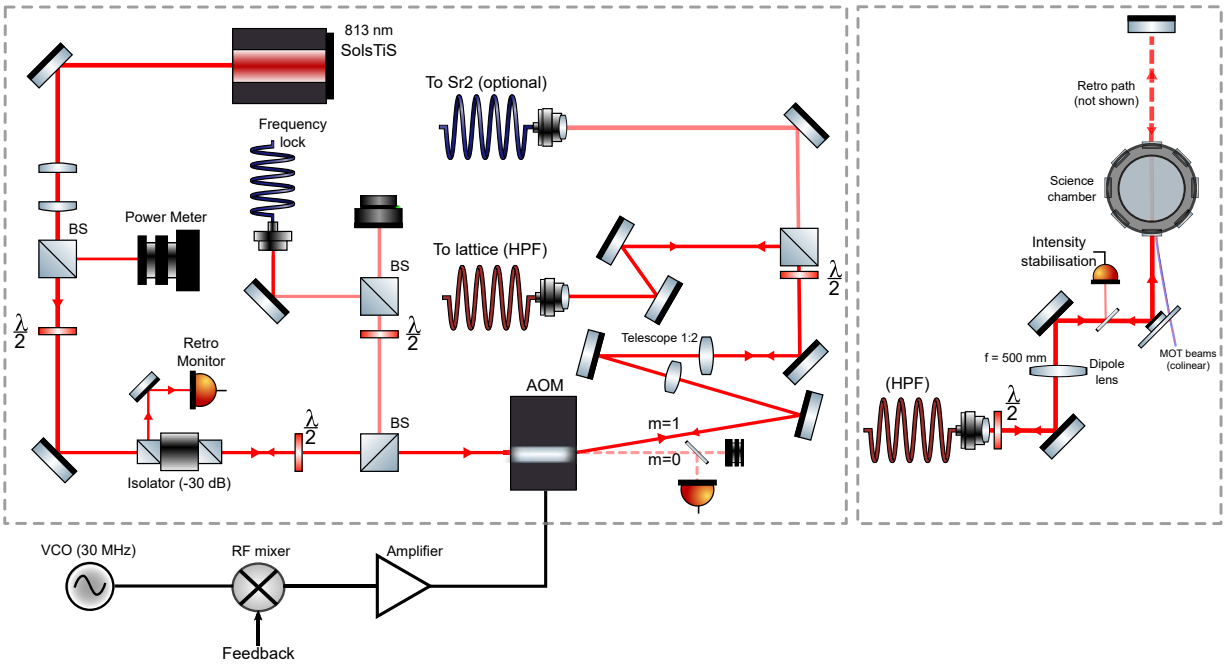

Figure 4.1: 813 nm SolsTiS set up used for the optical lattice. The in going lattice beam is intensity stabilised via an AOM prior to the high powered optical fiber to the science chamber.

The AOM somewhat distorts the gaussian beam profile of the wavefront which leads to a deterioration in fiber coupling efficiency. Typically 70% was achievable with some optimisation. The first order diffraction efficiency of the AOM was 85%. In order to operate the intensity stabilisation scheme discussed later in this chapter, it is important to leave some headroom in the diffracted power of the AOM. Therefore, the experiment is run at ∼10% below maximum power in the m=1 beam. Additionally, the SolsTiS was found to decrease in power by several 100 mW over the course of a day which can be accounted for by a lower set point in the intensity servo. Typical values of ∼3 W are measured after the fiber when these considerations are all met.

After the high power fiber the beam is collimating to a size of approximately 1 cm and focussed to the centre of the chamber using a 500 mm lens. It is reflected off a specially designed glass slide with a mirror placed in the centre, which allows the red and blue MOT beams to pass. As mentioned the lattice/clock beams are very slightly angled with respect to the horizontal MOT beams to allow for mirrors.

4.1.2 Retro path

The clock and lattice beams are separated at a special coated dichroic mirror whose coating passes 698 nm while reflecting 813 nm. A 500 mm lens collimates the in going beam and acts as the focusing lens for the retro reflected beam. A 10:1 telescope is used to shrink the beam down and a 50 μm pinhole aperture is placed at the focus. This ensures the returning beam, which has made four separate passes through AOM crystals is gaussian. It was found that the beam shape is extremely compromised on the return path without this addition. A small portion of the beam ($\ll 1\%$) is picked off prior to the AOMs to an amplified photodiode. This is then used to stabilise the in going beam power. It is important to stabilise the in going beam power using a photodiode after the fiber and as close to the atoms as possible to account for fluctuations in fiber coupling.

The beam then double passes a 30 MHz AOM pair. The beam takes the m=1 order at the first AOM and m=-1 order at the second. This ensures that the retro reflected beam has the same frequency as the incoming beam. This is vital to ensures the lattice frame is fixed[7]. Apertures are used to block the 0^{th} order after each AOM. A 99:1 pick off slide is used to monitor the retro beam after the final AOM. Once the AOMs are correctly aligned the retro path is aligned by a single mirror making this an extremely effective design. Additionally, a 'cat's eye' lens and $\lambda/4$ waveplate are used at to focus the beam on to the retro mirror. This negates the effects of beam divergence as the retro path is on the order of z_r.

4.2 Intensity stabilisation

4.2.1 Acousto optical modulators

An acousto optical modulator can be used to frequency modulate an incident beam. It is especially useful since unlike other forms of phase/frequency modulation the shifted and unshifted beams are displaced with respect to each other.

A resonant LC-circuit drives a piezo transducer causes sound waves to propogate across an

[7]so-called 'running' lattices can be created by shifting the incoming/retro beam frequencies with respect to each other

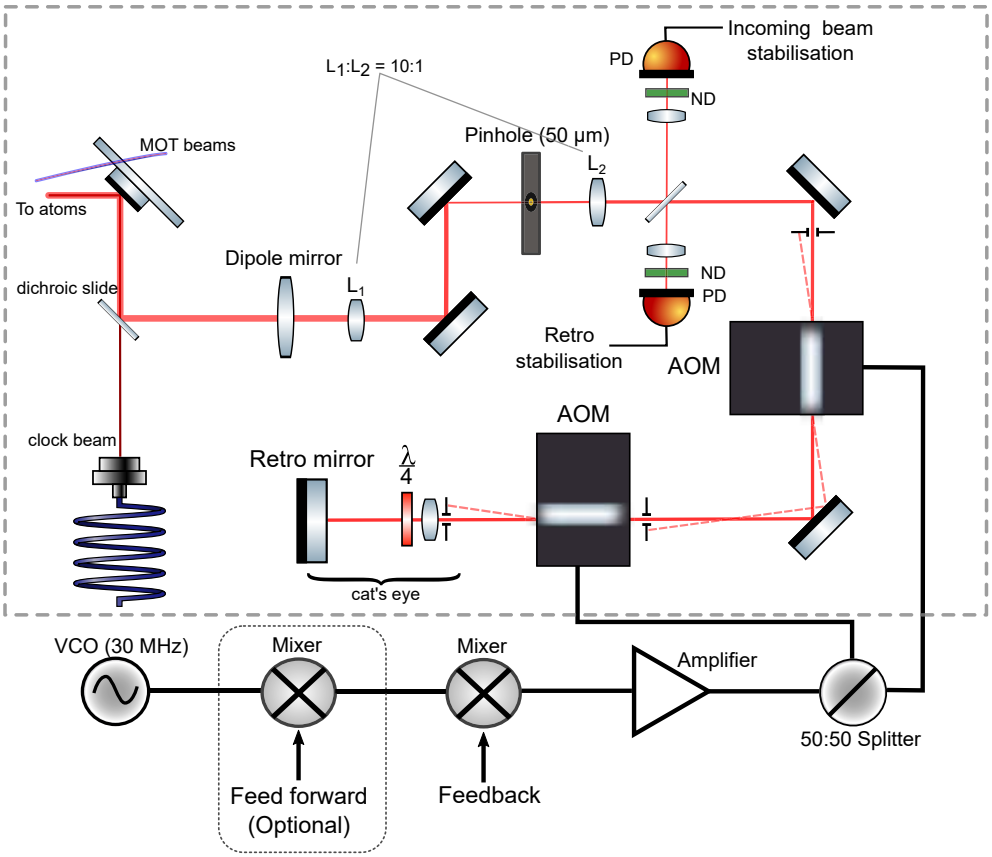

Figure 4.2: Retro intensity stabilisation and ramping: Two double passed AOMs are used to stabilised and ramp the retro reflected lattice beam. A feedback/feed-forward scheme is used to actuate a double-balanced mixer which acts as a variable attenuator for the 30 MHz RF source.

optically transparent crystal with a narrow frequency width. The sound propagating through the crystal creates regions of high/low refractive index in the crystal. These effectively form a diffraction grating with constructive inteference at $n\lambda_l = \Lambda_s \sin\theta_d$, where λ and Λ_s are the wavelengths of the light and acoustic waves respectively. Equivalently the shift can be thought of as being caused by gaining/losing phonons of momentum $\hbar k_s$ perpendicular to the beam.

The diffraction efficiency of the AOM is determined primarily by the power of the RF source

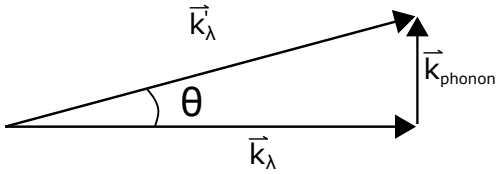

driving the piezo transducer. The relationship between driving power and the efficiency in the first order η is given by

$$\eta = \eta_0 \sin^2\left(\frac{\pi}{2}\frac{P}{P_0}\right) \qquad 0 \leq P \leq P_0 \tag{4.1}$$

where P and P_0 are the RF drive power and saturation power in Watts and η_0 is the maximum efficiency at saturation. Above saturation the relation is approximately flat until the damage threshold.

4.2.2 Analog servo overview

Figure 4.2 shows a basic overview of the intensity stabilisation scheme applied on the incoming and retro beams. The actuator in the servo loop is a double balanced mixer (DBM) (shown inset) which acts as a voltage controlled variable attenuator of the RF source. A DC current applied to the Intermediate Frequency (IF) port of the DBM controls the output. The RF is provided by a 30 MHz voltage controlled oscillator (VCO) with a maximum output power of 10 dBm.

A small portion of the beam is split off and a photodiode with transimpedance amplifier is used to measure the intensity. An analog servo system designed at JILA feeds back to the DBM and maintains the light intensity at a fix point controlled by an external set point, set by computer.

4.2.3 Analog servo control electronics

We will now discuss some of the important characteristics of our feedback system. We begin by considering the generic loop filter block diagram (figure 4.3) shown here as a reference to help characterise some of the features of our intensity servo design. It is customary to define the parameter $s = i\omega$ to allow us to consider the response of the system across any and all frequencies.

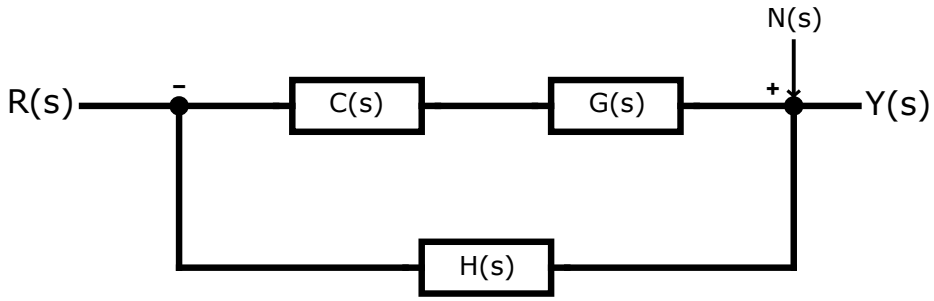

Figure 4.3: Negative feedback loop: shows schematically the relationship between output $Y(s)$ and set point $R(s)$. $C(s)$, $G(s)$ and $H(s)$ are the Laplace transforms of the controller, system and measurement responses respectively. An arbitrary noise spectrum is present with the Laplace transform $N(s)$.

The benefit of the Laplace transform is that unlike in the time domain, the transfer functions of the various subsystems are multiplicative. The output signal of the generic loop filter shown is given by

$$\begin{aligned} Y(s) &= \big[R(s) - H(s)Y(s)\big]C(s)G(s) + N(s) \\ &= \frac{C(s)G(s)R(s)}{1 + H(s)C(s)G(s)} + \frac{N(s)}{1 + H(s)C(s)G(s)} \end{aligned} \tag{4.2}$$

Clearly noise can be suppressed by designing a system where the loop gain, $H(s)C(s)G(s)$, is large, whereas the system becomes unstable at $H(s)C(s)G(s) = -1$. The system has a critical frequency ω_c above which it cannot respond defined by the loop delay time $\tau\omega_c = \pi$. At ω_c feedback is directly out of phase and noise is amplified. It is important that $|H(s)C(s)G(s)| \ll 1$ at $s = i\omega_c$.

A simplified circuit diagram for the analog servo for intensity stabilisation (full circuit found in Appendix) is shown. V_{set} is controlled externally by a computer and plays the role of $R(s)$. The photodiode voltage, V_{pd} is given by the product of our laser intensity with the

transfer function for the photodiode ($H(s)Y(s)$).

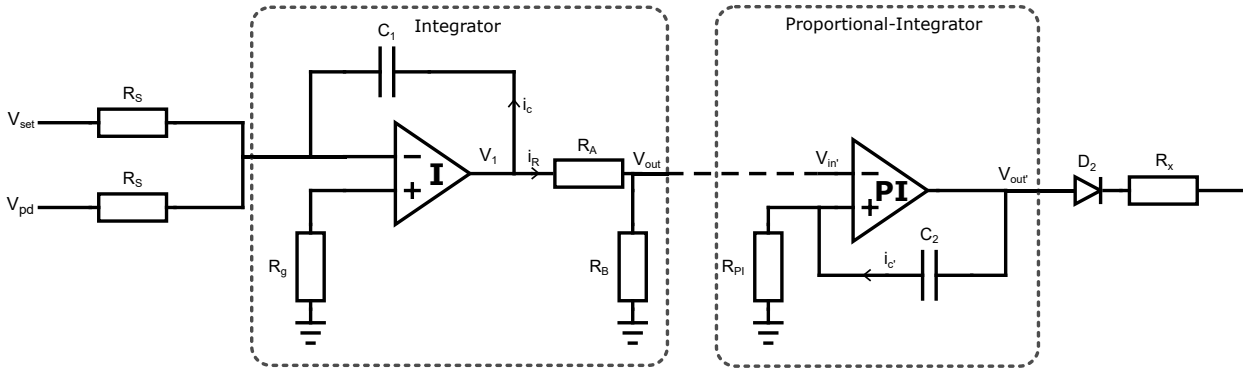

Figure 4.4: Simplified schematic of the JILA intensity servo. A double integrator has properties which are advantageous over the first order proportional-integrator controller. The servo actuates on the double-balanced mixer to attenuate the RF source driving the AOMs.

First we analyse the behaviour of the first op-amp making the standard assumptions of infinite impedance at the inverting/non-inverting inputs. We shall define $V_{in} = V_{set} + V_{pd}$ and not that by design V_{pd} is negative. V_{in} is therefore the error signal. The op-amp sees 0 V on the non-inverting input and therefore the output drives a current $I = i_c + i_R$ whose value cancels out V_{in}/R_s. Therefore

$$\frac{V_{in}}{R_s} = -i_c = I\frac{Z_R}{Z_R + Z_c}$$

where Z_c and Z_R are the impedance for the capacitor C_1 and the two resistors (here $Z_R = R_A + R_B$ since the impedance at the second op-amp is infinite). The voltage V_1 is given by $i_c Z_c$ and we can calculate the output of the first servo by

$$V_{out} = V_1\frac{R_B}{R_A + R_B} = i_c Z_c\frac{R_B}{R_A + R_B}$$

where we will refer to $\frac{R_B}{R_A+R_B}$ as the fine gain constant. Since we can write the current through C_1 in terms of our input voltage this allows us to write

$$V_{out} = -\frac{V_{in}}{R_s}\left(\frac{R_B}{R_A + R_B}\right)Z_c \tag{4.3}$$

where $Z_c = \frac{1}{i\omega C}$. We can now rewrite equation 4.3 to give us the transfer function $T_I(s)$ of the first part of our servo.

$$\frac{V_{out}}{V_{in}} = -\frac{1}{i\omega RC_1}\left(\frac{R_B}{R_A + R_B}\right) \propto \frac{1}{s} \tag{4.4}$$

This is the transfer function of an integrator. The response of the first stage of the servo falls off linearly with frequency, giving highest gain at lower frequencies. In essence it acts as a low pass filter.

The second stage plays the role of a proportional integrator. The output drives the non-inverting input to $V_{in'}$ and we find that

$$V_{in'} = V_2 = i_{c'} R_{PI'} = V_{out}\frac{R_{PI'}}{Z_c + R_{PI'}}$$

and therefore

$$T_{PI}(s) = \frac{V_{out}}{V_{in}} = 1 + \frac{Z_c}{R_{PI'}} = 1 + \frac{\kappa}{s} \tag{4.5}$$

The combined transfer function, $C(s)$ is given by $T_I(s)T_{PI}(s) = \frac{\kappa_{ii}}{s^2} + \frac{\kappa_i}{s}$. The double integrator (DI) has two distinct advantages over the more common proportional-integral controller. Firstly, it has higher gain at low frequencies. This is beneficial since most intensity noise is at acoustic frequencies. Secondly, the gain rolls off more quickly than in the single integrator case. Since the response of the AOM actuator in the intensity servo loop is time limited it dominates the critical frequency ω_c of the feedback loop. It is vital to have gain $\ll 1$ at ω_c to prevent ringing and decrease the "servo bump" - the region of additional sensitivity around ω_c where the controller actually amplifies system noise. This is tuned using the potentiometer R_1 and the fine gain constant set by R_A and R_B

The intensity servo drives the Intermediate Frequency (IF) port of a double balanced mixer whose attenuation is related to the magnitude of the current drawn. The resistor R_x is chosen such that the maximum current drawn is within the range of operation of the mixer (typically $\sim$ 0 - 10 mA. The op-amp should also be capable of supplying adequate current. Since the attenuation is only dependent on the magnitude of the current drawn, a diode

(D_1) is used to keep the servo response unipolar and gain sign positive.

4.2.4 Non-linear servo response

In the previous section we have discussed how our system responds to changing frequency, however, it is important to acknowledge that $C(s)$, $G(s)$ and $H(s)$ also depend on the laser intensity (i.e. the value of V_{set} ($R(s)$)). This means that in general the loop properties will not be the same at two different intensity set points.

For the intensity servo we ensure linearity by operating in the linear regime for i) the chosen op amps ii) the output diode. In effect this means that κ_{ii} and κ_i are independent of the set point. While some non-linearity persists, the circuit can be implemented so these are negligible by correct choice of components.

Unfortunately, the response of our system, $G(s)$, is inherently highly non-linear. The gain is proportional to the gradient of the intensity/voltage curve for servo output voltage. This is comprised of the response of the AOM (given in equation 4.1) and the mixer. If the set point for the intensity controller needs to be changed, as in the case of lowering/raising the lattice depth, then $H(s)C(s)G(s)$ needs to be acceptable over the full range of intensities being swept through. One way to improve this problem in the case of ramping the intensity is to model the non-linearities and account for them using a feed-forward scheme. We discuss this process in section 4.5.

4.2.5 Photodetector and control signal

The photodetectors used for intensity stabilisation were transimpedance amplified Si photodiodes[8]. These have very good linearity across several orders of magnitude and are shot noise limited across a range of $\sim 5 \times 10^2$. The voltage set point of the servo is set via a digital data acquisition device. One downside of using a digital set point is the presence of high frequency noise (∼100 kHz) from the DAQ's in built clock and discrete voltage steps. Also DAQs suffer from glitching when they step from a voltage assigned to an all 1s bin to a primarily 0s bin. These can be seen as high frequency spikes on an oscilloscope trace due to

[8]The interested reader can find an extensive description of their design in [46]

overshooting the programmed voltage. These were resolved by low pass filtering the output waveform from the DAQ well below the clock frequency. Low pass filtering the reference value does not effect the servo bandwidth, however the -3 dB point of the filter needs to be chosen well above any Fourier frequencies of the set point ramp.

4.2.6 Analog Servo Performance

The ideal intensity servo should achieve shot-noise limited performance. The shot noise for a given intensity is Poisonian and the r.m.s. current fluctuations due to shot noise are be given by

$$\sigma_i = \sqrt{2eI_p\Delta f} \tag{4.6}$$

where I_p is the photocurrent, given by $I_p = \mathcal{R}(\lambda)P$, P is the incident power and Δf is the relevant bandwidth interval. The photocurrent fluctuations are mapped on to voltage noise via the gain of the load resistor or trans-impedance amplifier. The photodiodes we use to stabilise both lattice beams perform at the photon shot noise limit at the relevant intensities (see reference [46]) with any additional noise being due to the loop filter.

To measure the performance of the loop, a thermal light source (an incandescent light bulb) was used to register an equivalent photocurrent (light intensity) to the laser beam and the noise spectrum was recorded using a low noise FFT machine. The noise spectrum agrees with calculations of the shot noise for this intensity. Next, the laser was tuned to the same intensity and stabilised. We used identical photodiodes to record the "in-loop" and "out-of-loop" noise spectrum (figure 4.5).

The increased noise in the in-loop spectrum comes is the well understood 'servo bump' described above and is not present in the out-of-loop signal. Noise spikes at ∼15 kHz, ∼20 kHz and ∼40 kHz are caused by other sources in the lab. They are present on the in-loop and out-of-loop spectra due to pick up on the longer cables used for these two measurements. The servo electronics were moved closer to the photodiodes to reduce this noise.

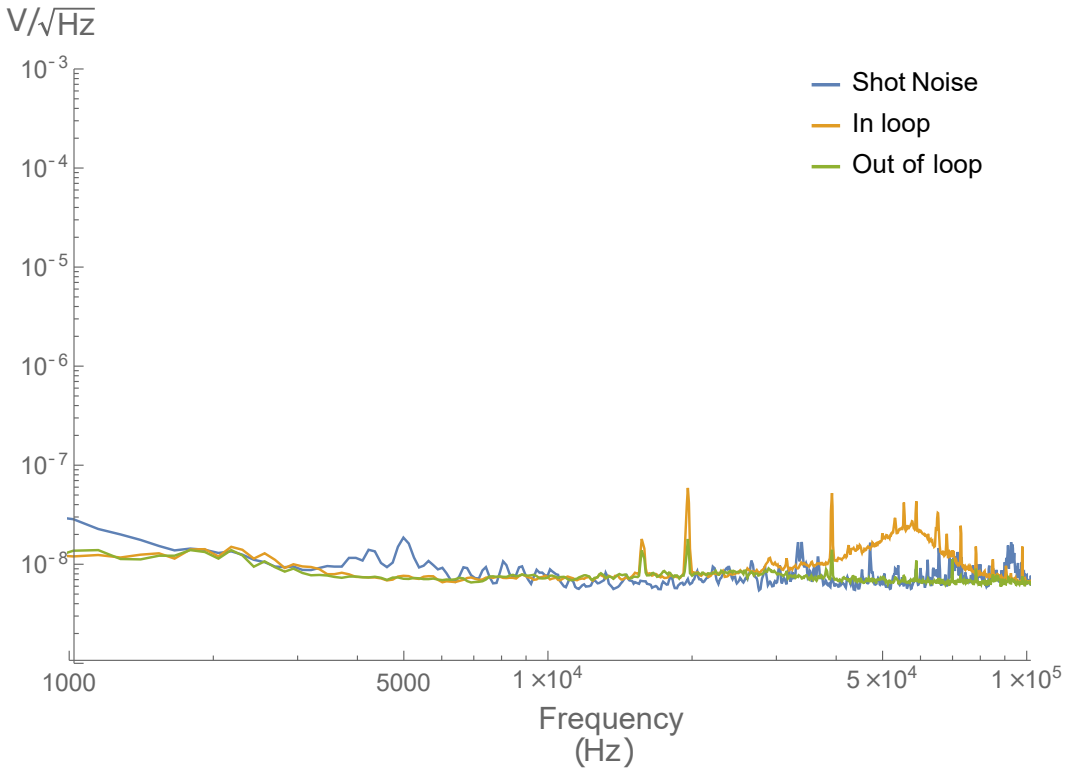

Figure 4.5: In-loop and out-of-loop performance of intensity stabiliser. Shot noise consistent with 10 nV/$\sqrt{\text{Hz}}$ as per calculation. The servo bandwidth for this data was 60 kHz.

4.3 Bandwidth

4.3.1 Limitations on ω_c

The loop delay for the intensity stabilisation scheme discussed here is only fundamentally limited by the transit time of sound waves in the AOM. The intensity in the diffracted order can only respond as fast as the soundwaves can propogate i) from the transducer to the beam ii) across the finite width of the laser beam. In applications where the loop bandwidth should be maximised the beam should propogate as close to the transducer and possible and be tightly focussed inside the acousto-optical crystal. It is possible to achieve critical frequencies of several MHz in this way[9]. However there are many more considerations when dealing with electronics (for examples op-amps) with bandwidths in the MHz range. The intensity servo described here is limited to a maximum bandwidth of 100 kHz by the RC constant of the first integrator. This limits ω_c but prevents the system becoming unstable. It also allows a much larger beam size through the AOM without diminishing response time,

[9]note that the response of the AOM can never exceed $f_{mod}/2$ where f_{mod} is the modulation frequency

which allows high power beams to be stabilised without reaching the damage threshold for the crystal.

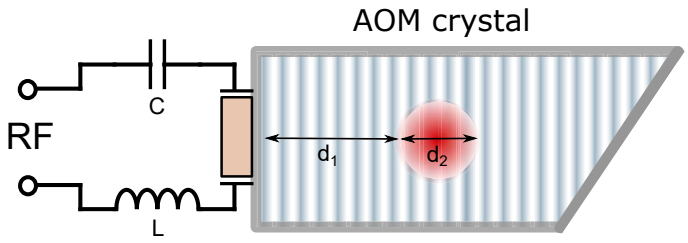

Figure 4.6: The time delay between the piezo transducer is characterised by the sound travel time across d_1, the distance of the beam from the transducer and d_2, the beam diameter. These physical dimensions bound ω_c.

4.3.2 Parametric heating

As mentioned, the servo causes amplification of noise at frequencies close to ω_c. Atoms trapped in the lattice are sensitive to intensity fluctuations only at certain frequencies. If the servo bump coincides with such frequencies then the transition rate between motional levels of the trap are increased and the atom sample is heated.

In the pseudo-harmonic trap the transition rate from motional state $|n\rangle \rightarrow |m\rangle$ is given by

$$W_{m\rightarrow n} = \frac{M^2{\omega_z}^4\pi}{4\hbar^2}\left|\langle m|\hat{x}^2|n\rangle\right|^2 S_N(\omega_{n\rightarrow m}) \tag{4.7}$$

where $S_n(\omega_{n\rightarrow m})$ is the noise power spectral density in the electric field at the relevant transition frequency, ω_z is the axial trapping frequency and $\hat{x} = \sqrt{\frac{\hbar}{2M\omega_z}}(\hat{a} + \hat{a}^\dagger)$ is the position operator in terms of the creation and annihilation operators. The matrix element $\langle m|\hat{x}^2|n\rangle$ is only non-zero for transitions where $m = n \pm 2$, meaning that our system is maximally sensitive to intensity fluctuations at $2\omega_z$.

The intensity servo was required to operate at both high ($w_z \sim 2\pi \times 100$ kHz) and low ($w_z \sim 2\pi \times 20$ kHz) trap frequencies. This ultimately led to the servo bandwidth being deliberately reduced to 10 kHz. This was suitably high to i) suppress most low frequency, acoustic and vibrational noise sources ii) enable the intensity set point to be ramped on 1 ms timescales. Alternatively, the servo bump could have been set $\gg \omega_z$ if noise at the

trap frequency needed to be suppressed more. This would require a faster electronics and optimising the loop frequency as described above.

4.4 Dynamic ramping

The ability to dynamically ramp the intensity during an experimental cycle adds a valuable new tool to probe the lattice interactions. One reason to ramp the lattice is to utilise the Lamb-Dicke confinement of the deep lattice for precise spectroscopic readout while allowing evolution in the weak lattice where spin-orbit coupling becomes prevalent see section 5.5.5. Indeed one proposal for measuring the modification of spin-orbit coupling involves a Ramsey spectroscopy scheme where atoms spend the dark time in the spin-orbit coupling Hamiltonian and the accumulated phase is measured by ramping back to the deep lattice for the readout pulse. In such a scheme the lattice intensity must be ramped suitably slowly so that eigenstates of the strongly confining lattice evolve adiabatically. The population of each energy band should, for example, be preserved.

The condition for adiabaticity in the motional groundstate of a lattice with depth V is given by [47]

$$\left|\langle n,q|^{\partial}/_{\partial t}|0,q\rangle\right| \ll \left(\frac{E_n(q') - E_0(q)}{\hbar}\right)^2 \tag{4.8}$$

where n is the motional band index. This condition is clearly most stringent i) for transitions to n=1 ii) at the Brillouin zone edge $|q| \to \hbar k$ and iii) in the weak lattice case where band spacing is small. In the tight binding approximation, the energy gap $E_n(q) - E_0(q)$ is linear in V_0 at the Brillouin zone edge and we find that $\partial V_0/\partial t \propto V_0$ such that the adiabaticity varies exponentially with lattice depth V_0. At a trap depth of $V_0 = 14\ E_r$ the band spacing is $\sim \hbar \times 2\pi \times$ 50 kHz. If we assume a factor of 10 difference in the Fourier frequency of our ramp to ensure adiabaticity and set

$$\left.\frac{1}{E_r}\frac{\partial V_0}{\partial t}\right|_{V_0=14E_r} = 5\text{kHz}$$

which allows us to calculate a time constant $\tau = 3.5$ ms for the exponential intensity ramp which satisfies the condition $\dot{\omega} = \frac{1}{10}\omega^2$. A factor of 10 is a minimum requirement and in a

ramp of $\tau \sim 100$ ms is used. For a linear ramp, the gradient should satisfy the adiabaticity at the lowest lattice intensity.

We neglect radial modes in the adiabaticity calculation for two reasons: firstly, the physics we are interested in studying occur in the axial modes and there is negligible axial-radial coupling and secondly, the spectrum of radial modes is not discrete as in the case of the axial direction.

One can also imagine scenarios where we might want to study the non-equilibrium dynamics of a sudden quench of the system. This can be achieved by very quickly (diabatically) switching the lattice intensity from high to low. It is therefore a useful tool to be able to control the lattice intensity at much faster timescales too.

4.5 Feed forward/feedback

The use of feed-forward can drastically improve the performance of a negative feedback control system in which the set point ($R(s)$) is time varying. Feedback systems alone are purely reactionary, their performance being limited by the loop bandwidth and the gain curve. Without prior knowledge, a sudden change in the set point results in a large deviation in the error signal $R(s) - H(s)Y(s)$. The system may stray unacceptably far from the desired value. In the worst case high gain can cause the system to become temporarily unstable or come 'out of lock', deviating beyond the capture range of the servo.

Feed-forward is a way to negate this effect. An out of loop signal $F(s)$ is used which creates the correct response from the system at the output ($F(s)G(s) \approx Y(s)$). The feed-forward signal is synchronised with the changing set point. Since the system is already being steered in the correct direction by feed-forward the error signal is drastically reduced and the system experiences much smaller excursions from the desired value, constituting a tight lock.

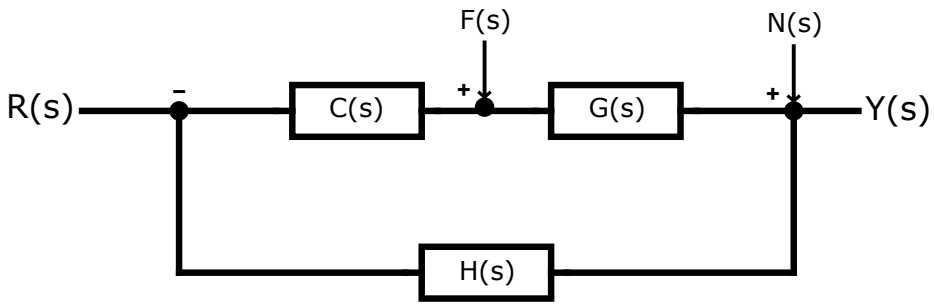

Figure 4.7: Feed-forward/feedback control block diagram. The feed-forward function $F(s)$ is synchronised to changes in $R(s)$ and prevents large excursions from the set point causing instability in the loop.

4.5.1 Feed-forward methods

Two methods were explored for providing feed forward for ramping the intensity using the intensity servo.

- **Summation of control signals**

  Addition of the feed-forward signal and the control signal can be done directly as shown in figure 4.8 using a summing amplifier. However, since the intensity servo is unipolar it must be modified by moving the diode after the summing amplifier, in effect making the feedback control bi-directional but driving a uni-directional current through the DBM. Additionally, the summing amplifier modifies the loop gain by a factor g_+.

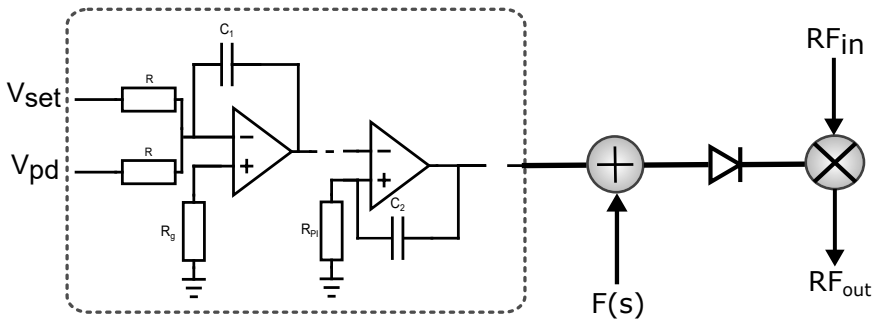

Figure 4.8: Feed-forward using a summing amplifier

- **Two double balanced mixers**

  Another alternative is to add a second double balanced mixer. This can be used as a voltage controlled attenuator, modifying the RF power into the second mixer which

is actuated on by the servo. For a fixed servo output current (and therefore fixed attenuation) the first mixer controls the laser intensity by modulating the RF power available and therefore the diffraction efficiency at the AOM.

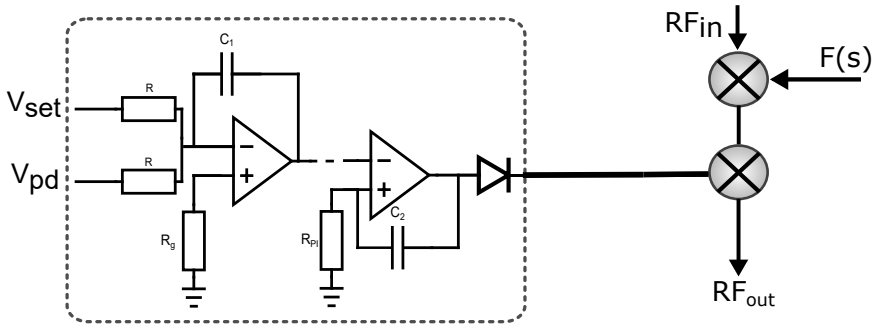

Figure 4.9: Feed-forward using two double balanced mixers

4.5.2 Fitting non-linearities in feedback loop

In order to use feed-forward to steer the output (laser intensity) we must understand the transfer function of our system. As mentioned, both the double balanced mixer and the AOMs are highly non-linear devices. To simplify this process it is important that the output diode and RF amplifiers/attenuators are working in the linear regime where possible. This can be achieved by correct design and choice of components.

The first order diffraction of an AOM is given by

$$\eta = \eta_0 \sin^2\left(\frac{\pi}{2}\frac{P}{P_0}\right) \qquad 0 \leq P \leq P_0$$

where P and P_0 are the RF drive power, and saturation power in Watts. η_0 is the diffraction efficiency at saturation (approximately 85 %). The behaviour of the double balanced mixer can be well approximated by

$$\xi = \frac{\xi_0}{1 + e^{-k_1(V - V_{1/2})}}$$

where ξ is the linear efficiency, $V_{1/2}$ is the -3 dB voltage and k_1 is an unknown constant related to the behaviour of the quad diode ring in the DBM. Experimentally we desire to ramp only the retro beam in order to vary the axial trapping frequency. This means that we must consider all four AOM passes which introduces a $\sin^8(\dots)$ term. The overall transfer function is modelled as

$$\eta = \eta_0 \sin^8\left(\frac{\pi}{2P_0}\frac{1}{1+e^{-k_1(V-V_{1/2})}}\right) \qquad 0 \le P \le P_0 \tag{4.9}$$

where I_0 is the laser intensity when the mixer attenuation is ξ_0 and the intensity in the m=1 order is given by $I = \eta I_{in}$. The voltage at the IF port of the double balanced mixer is varied using manual control of the intensity servo output (see Appendix for details) and the resulting laser intensity is measured at a photodiode. The photodiode voltage, $V_{pd} \propto$ I is recorded and the resulting curve is fit with the model in equation 4.9 (figure 4.10).

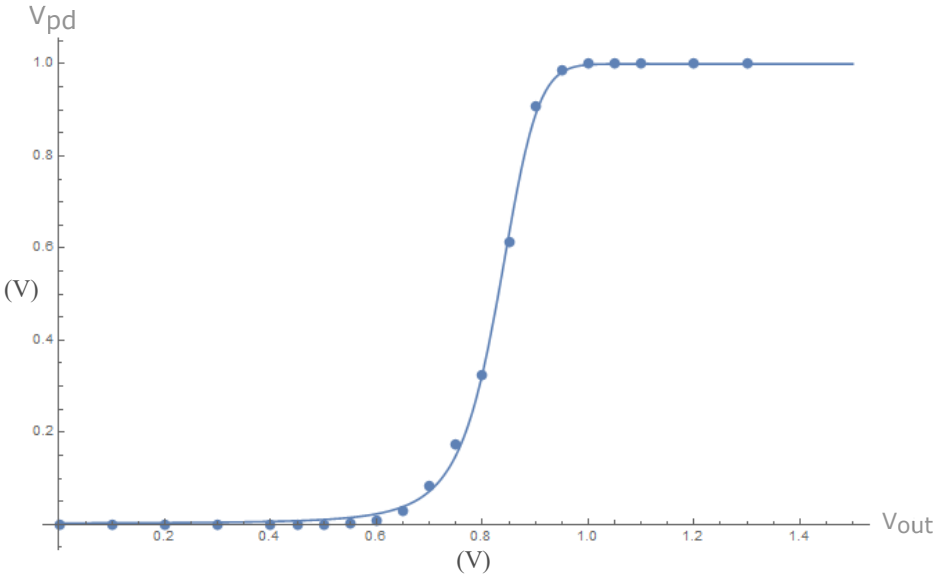

Figure 4.10: Modelling the non-linear behaviour of the mixer and AOMs in the loop. The servo output voltage is varied linearly and the photodiode voltage (proportional to the intensity) is recorded. A good fit to the data was found, indicating that the form of the transfer function was approximately correct.

The transfer function can be inverted and used to find the feed-forward function $F_V\big(V(t)\big)$ to produce any arbitrary intensity ramp $I_R(t)$ (see Appendix A). For the retro path the formula for calculating arbitrary ramps is

$$F_V(t) = \frac{1}{k_1}\left[\ln\left[\frac{2P_0}{\pi}\sin^{-1}\left(\frac{I_R(t)}{I_0}\right)^{-\frac{1}{8}} - 1\right] + V_{1/2}\right]$$

Using this method we were able to generate any ramp shape we desired. The intensity could be swept through a range of $\approx 10^3$ whilst servoing with stable feedback. This was limited by a 10 mV combined offset from the inverting/non-inverting inputs of the op-amp in the transimpedance amplifier and the 0 V output of the DAQ which was a few mV above

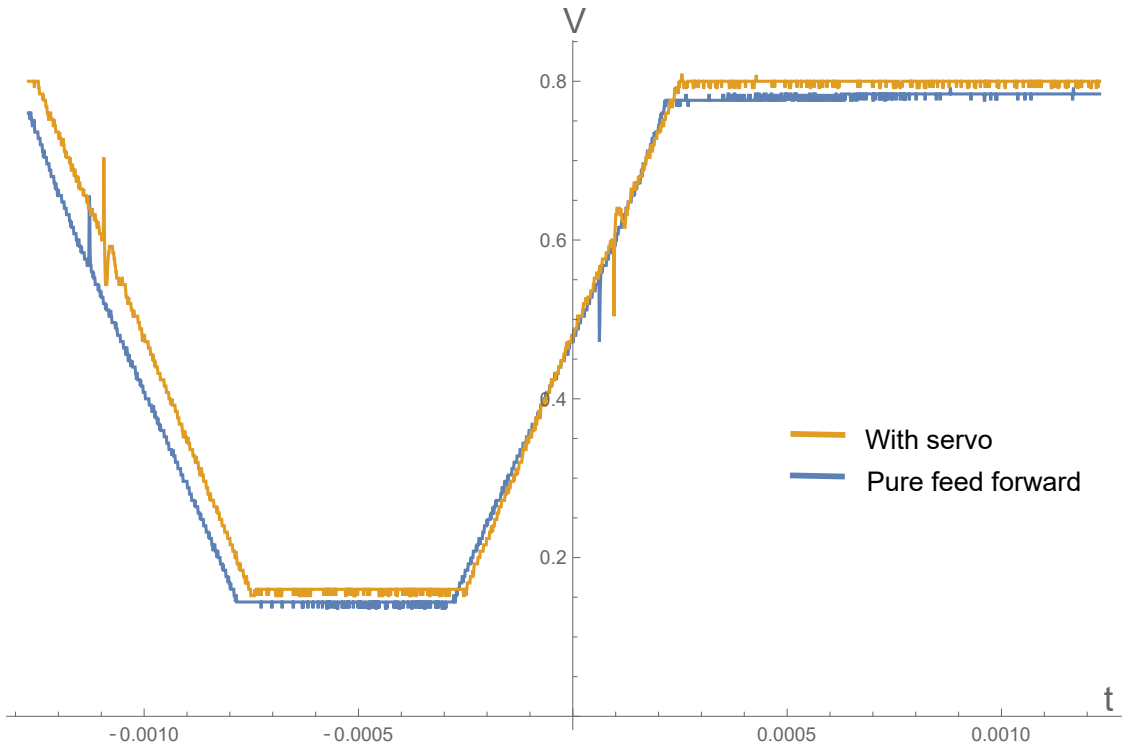

Figure 4.11: Feed-forward proof of concept. The feed-forward function can be used to generate an almost perfect intensity waveform. This dramatically reduces the load on the servo loop. Noise spikes at 0.6V are due to the DAQ 'glitching' and are solved with a simple low pass filter.

ground. In practise the DAQ output can be calibrated to take account for the offsets, but the magnitude of the offset is found to fluctuate by several mVs. The upper end of the dynamic range is limited by the saturation of the photodiode.

Figure 4.11 shows the feed-forward signal being used to control the output intensity. A 0.5 ms linear ramp between two intensities is run with/without the servo to demonstrate how closely the feed-forward system can generate the desired waveform. The disturbances at ∼0.6 V is caused by 'glitching' in the DAQ and can be eliminated using filters.

4.5.3 Advantages of feed-forward

With the feed-forward in place scheme it was possible to perform ramps as fast as 50 μs from maximum to minimum power with almost perfect linearity. This is well beyond the scope required for any current experiments but could open up an interesting way to reliably switch on/off a potential diabatically -as in a sudden quench.

Feed-forward was also found to drastically improve the system's response to step changes in the set point, with settling times reduced by a factor of 20. For linear ramps (e.g. a triangular wave) the basic feedback system was found to deviate from the set point and oscillate momentarily at the top and bottom of the ramp where the second derivative of the diverges. This problem is solved by using feed-forward since the output responds deterministically to the feed-forward signal as the set point is rapidly changed. Therefore the error signal is small and the servo responds less aggressively.

4.5.4 Possible improvements

The feed-forward system described improves the servo response to sudden changes by reducing the deviation between the output and the set point using prior knowledge of the change. It does not however correct for the non-linear features of $G(s)$ which change the loop gain as a function of V_{set}. Shown below (figure 4.12) is an improved system which can compensate for the non-linearites and keep the gain characteristics of the feedback loop fixed with intensity.

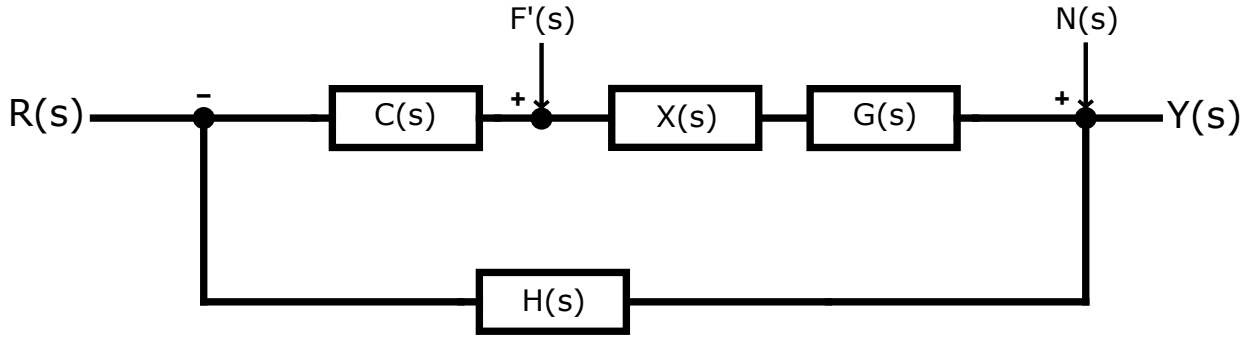

Figure 4.12: An improved feed-forward design. The block $X(s)$ compensates for the non-linearities in $G(s)$ and flattens the gain across all values of output (laser intensity). $F'(s)$ is the modified feed-forward curve.

Here we introduce a new block $X(s)$ whose purpose is to linearize the output of $G(s)$ across all voltages such that $X(s)G(s)$ is independent of intensity. By linearizing the output of $G(s)$ we do not elliminate the benefits of feed-forward, however we now use the feed-forward function $F'(s)$ which is simply proportional to the desired output intensity and no longer requires inverting the non-linear transfer function model (equation 4.9). In this new set up, our loop gain is constant across the full dynamic range and we need not compensate for the varying gain when tuning the servo.

Another desireable improvement is to further increase the dynamic range of the intensity servo. A variety of methods for doing so were tested. The most promising were i) to monitor the intensity using two photodiodes with different gains; the high gain photodetector is saturated and only becomes active during very low light intensity with an RF switch used to quickly ($t \ll 2\pi/\omega_{loop}$) switch which channel feeds back to the controller ii) a logarithmic photodiode can be used to prevent photodiode saturation whilst keeping the feedback signal within the useful range of the servo. Using two photodiodes operating in the linear regime causes a step change in loop gain. The logarithmic detector also changes the loop gain with intensity and requires that $X(s)$ have an exponential nature to compensate.

The correct way to implement $X(s)$ is debateable. An analog circuit could be designed with the desired functional form or the correct output could be calculated digitally. However, it should not introduce any delay in to the system or drastically change its frequency response. It should therefore have a bandwidth significantly larger than the critical frequency of the original loop.

5 Quantum Simulation and Spin-Orbit Coupling

This section seeks to motivate and provide details of ongoing work at JILA in which the author assisted. Plots from [1] are used with the authors' permission.

5.1 The Fermi-Hubbard model

Fermions in optical lattices offer a regime in which to study many aspects of the behaviour of 'real world' materials. The Fermi-Hubbard model, a powerful tool for describing the electronic properties of real solids, can be simulated in the optical lattice with neutral atoms. In the optical lattice, relevant physical parameters are highly tunable and offer the possibility to thoroughly map out phase transitions in parameter space in ways traditionally unavailable to condensed matter physicists.

The Fermi-Hubbard Hamiltonian has the form:

$$H = -J \sum_{\langle i,j \rangle,\sigma} (\hat{a}^{\dagger}_{i,\sigma} \hat{a}_{j,\sigma} + c.c) + U \sum_{i} \hat{n}_{i,\uparrow} \hat{n}_{i,\downarrow} \tag{5.1}$$

where i,j represent lattice site and the notation $\langle i, j \rangle$ denotes that the sum is taken over adjacent sites (i.e. in the 1D case $|i - j| = 1$). $\sigma \in \{\uparrow, \downarrow\}$ counts the spin species. The kinetic energy term in the Fermi-Hubbard Hamiltonian essentially describes electrons (atoms) hopping from lattice site to neighbouring lattice site at a tunnelling rate J, while the second term describes on-site interactions between particles. In the model, the Pauli Exclusion Principle precludes more than one of each spin species on a single site, although in optical lattices a single site may contain many more than one of a single spin species, with the degeneracy lifted by occupying different radial modes of the trap.

The interaction energy for two particles on a single site may be approximated as

$$U = g \int_{-\infty}^{\infty} \delta^3 r \left| w(\mathbf{r}) \right|^4 \tag{5.2}$$

where $w(\mathbf{r})$ is the Wannier function for an atom on a single site In the 1-D lattice the radial

parts of the wavefunction are the appropriate solutions to the Gaussian potential[10]. For systems where s-wave interactions dominate the coupling constant g is given by $g = \frac{4\pi a}{m}$ where a is the scattering length. For spin polarized fermions, as used in the ^{87}Sr OLC, calculation of the coupling constant is less straight forward and requires evaluation of the p-wave scattering volumes for the relevant symmetric and anti-symmetric pairings [34, 35].

For the purposes of this work it suffices to say that experimentally the on-site interaction energy U can be tuned by varying the density with which the optical lattice is loaded. Typically this is done by deliberately loading the MOT more or less efficiently to trap a greater or smaller number of atoms per lattice site. The tunnelling rate J can be experimentally tuned by controlling the depth of the periodic potential. This allows the parameter space for $^{U}/_{J}$ to be extensively explored[11].

5.2 Clock transitions in a weak lattice

In a deep lattice we have seen that atoms are in the Lamb-Dicke regime. The atom's internal state is decoupled from its momentum and the motional band structure is very well approximated by harmonic oscillator levels, with transitions from $|g, n\rangle$ to $|e, n \pm 1\rangle$ occuring at $f_0 \pm \nu_z$ for all atoms, where f_0 is the clock frequency.

When $\nu_z \gtrsim 40$kHz the site to site tunnelling time $1/J$ is sufficiently long with respect to experimentally relevant time scales that we can describe the physics of the transition with the single particle, strong confinement model, with atoms fixed to their lattice sites. In this case, the clock transition is seen as a narrow spectral peak when driven with a Rabi π-pulse. As the lattice strength U_z is weakened the width of the Rabi lineshape increases and two distinct peaks are observed instead of the single peak at f_0. To understand these features we begin by considering transitions from $|g\rangle \rightarrow |e\rangle$ where the tunnelling rate and subsequently the width of the lowest motional band is non-negligible.

The momentum of the incoming photon absorbed by the atom in transitioning from $|g, 0\rangle \rightarrow$

[10] It is common to approximate the potential as harmonic in the radial direction.

[11] Note that U and J are not entirely independent parameters since the spatial wavefunction overlap depends on the confinement

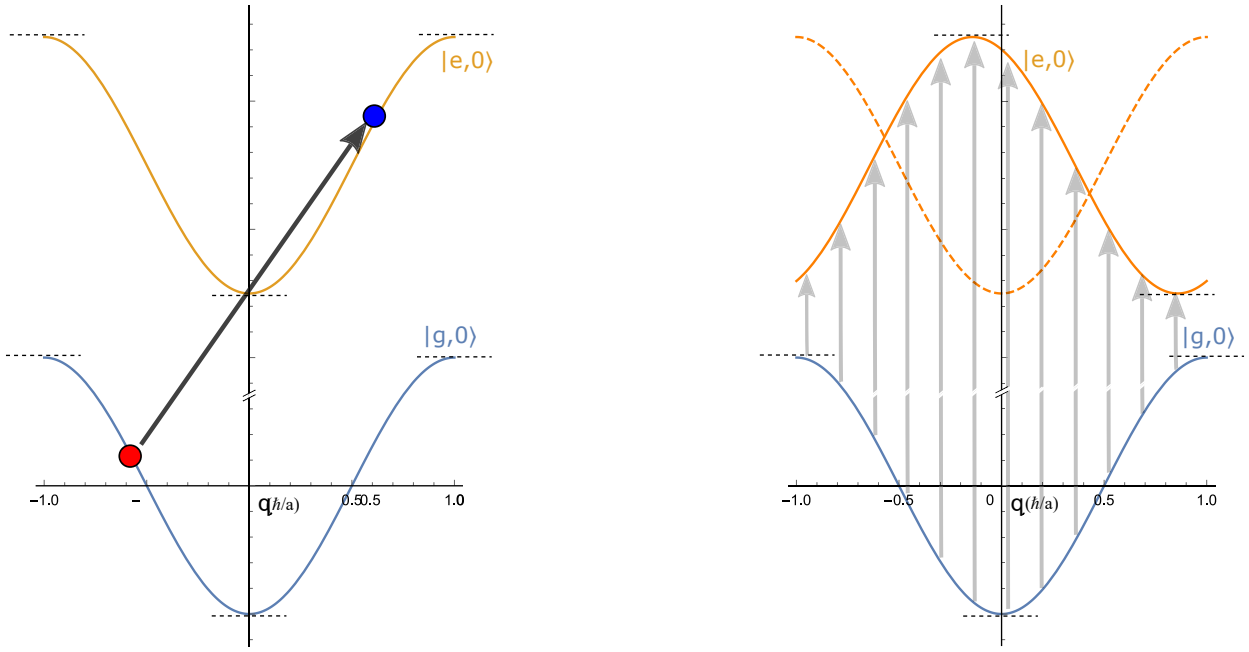

Figure 5.1: Transitions from the ground $|g,0\rangle_q$ to $|e,0\rangle_q$ in the weak lattice. (Left) The clock momentum $\hbar k_c$ is conserved by shifting the quasimomentum. (Right) The $|e,0\rangle_q$ band is shown shifted by $\phi = \pi\frac{k_c}{k_L}$ so that transitions are represented vertically. The finite bandwidth leads to a quasimomentum dependent detuning. Van Hove singularities occur at the turning points in the dispersion curves where the density of states diverges.

$|e,0\rangle$ is conserved by changing the final quasimomentum of the particle. The final quasimomentum is given by $q_2 = q_1 + \hbar k_c \pmod{2\pi}$. Where the $(\text{mod } 2\pi)$ denotes that we are working in the reduced brillouin zone. The left-hand side of figure 5.1 shows an atom transitioning $|g,0\rangle \rightarrow |e,0\rangle$. On the right-hand side the $|e,0\rangle$ band has been shifted by $k_c/k_L \approx -7/6$ so that transitions are shown by vertical lines. The transition frequency in going from $|g,0\rangle \rightarrow |e,0\rangle$ is dependent on the initial value q_1 of the atom and there is therefore a quasimomentum dependent detuning from the infinite confinement transition frequency f_0.

For the lattice depths relevant in this work the band structure of the lowest motional band (here called $|n=0\rangle$) is very well approximated (see Appendix C) by sinusoidal functions of the form

$$\Delta E^{(0)}_{q,\sigma} = E^{(0)}_{0,\sigma} - 2\hbar J\cos(\hbar q) \tag{5.3}$$

where $\sigma \in \{\uparrow, \downarrow\}$ and $E^{(0)}_{0,\sigma}$ is the energy at the centre of the band (i.e. $E^{(0)}_{q,\uparrow} - E^{(0)}_{q,\downarrow} = \hbar\omega_c$) where ω_c is the bare clock transition. Since transitions cause a phase shift in the band of approximately π, the $|e, 0\rangle$ band is nearly exactly inverted relative to the $|g, 0\rangle$ band for a vertical transition and therefore width of the distribution is given by $\Delta \approx 8J$.

The density of states is $\propto (\delta E/\delta k)^{-1}$ and diverges at the turning points of the dispersion curves. Consequently, most atoms lie in one of two distinct quasimomentum and the probability distribution of transitioning $|g, 0\rangle \rightarrow |e, 0\rangle$ is sharply peaked at the corresponding detunings. These divergences in the density of states are known as Van Hove singularities and can be observed in the absorption spectrum of crystalline solids and scanning tunnelling microscopy.

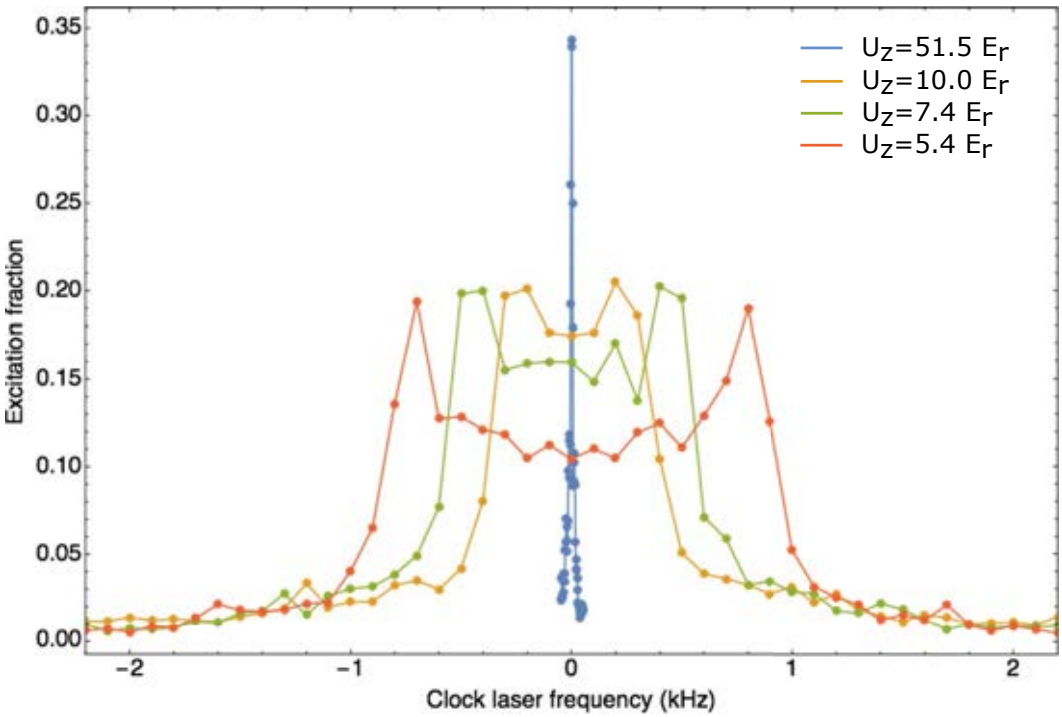

Figure 5.2: Rabi spectroscopy of clock transition in weak lattice. The normalised excited state fraction is used to measure transition probability. Shown are lattice depths of U_z = 51.5 E_r, 10.0 E_r, 7.4 E_r and 5.4 E_r. The sharp peaks in the distribution arise from the density of states which is sharply peaked at q^*.

Figure 5.2 shows the resulting atomic lineshape as the lattice depth is lowered. The frequency of the clock laser is detuned using an AOM and a Rabi π-pulse is used to drive atoms to the excited state. The distribution comprises both the detuning arising from the finite bandwidth and the peaks from the Van Hove type singularities in the density of states

which occur at q^*. Correspondingly, it is a convolution between the transition density of states and the Rabi lineshape for a single atom, on resonance transition.

5.3 Bloch band selection

One of the most powerful elements of using the clock state to probe the behaviour of the Bloch bands is the ability to use the clock architecture to purify atoms in a particular motional band. This allows us to directly compare behaviour in different bands for the same lattice conditions. As described earlier, we expect that the tunnelling rate J_n will be much higher in higher motional bands. This can be experimentally verified by recording the Rabi transition lineshape for identical lattices in both the $|n = 0\rangle$ and $|n = 1\rangle$ bands.

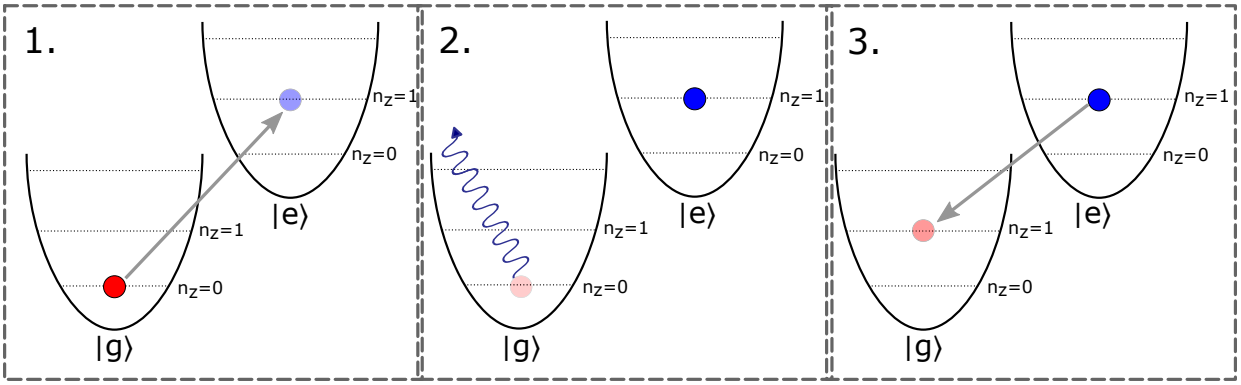

Figure 5.3: Procedure for purifying in the $|g, 1\rangle$ Bloch band. Atoms are excited on the blue sideband of the clock transition, remaining groundstate atoms are removed with a strong clearing pulse before the atoms are returned to the groundstate on the carrier transition. This allows the $n = 1$ band to be mapped as a function of lattice depth.

To do this, the atoms are prepared in a deep lattice and driven on the blue sideband (described in section 3.4) to the excited state $|e, 1\rangle$. Any atoms remaining in the groundstate are removed with a strong clearing pulse which removes them from the lattice but leaves the excited state atoms unperturbed. The atoms in $|e, 1\rangle$ can be brought back to the groundstate with a π-pulse on the bare f_0 clock transition $|e, 1\rangle \rightarrow |g, 1\rangle$. This is shown schematically in (figure 5.3)

(Figure 5.4) shows the Rabi lineshape of transitions $|g, 0\rangle \rightarrow |e, 0\rangle$ and $|g, 1\rangle \rightarrow |e, 1\rangle$ in four

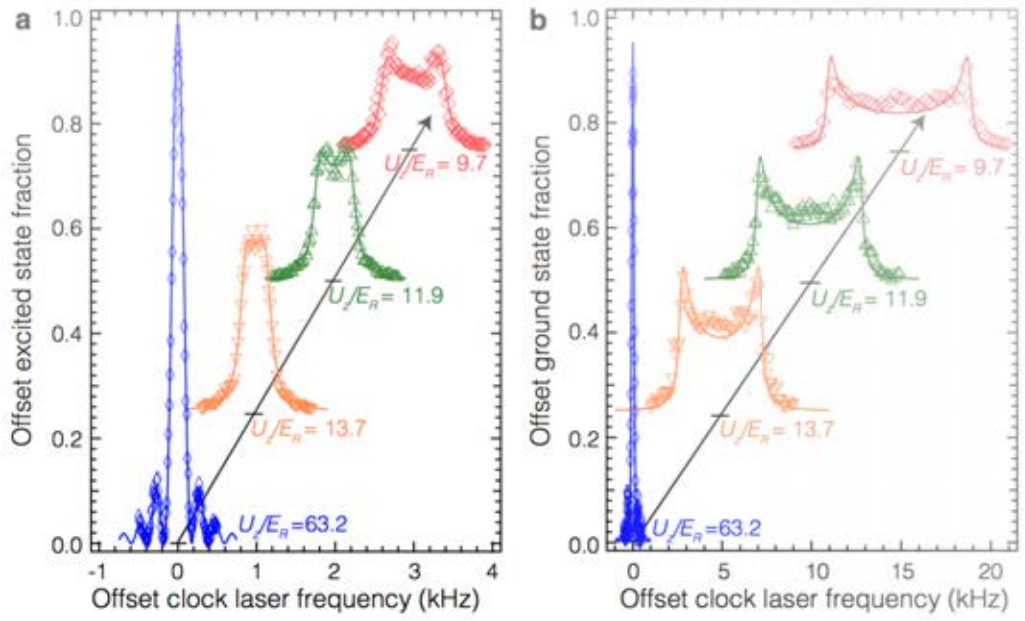

Figure 5.4: Rabi lineshape for lattice depths of 63.2 E_r, 13.7 E_r, 11.9 E_r and 9.7 E_r are probed for the $n = 0$ and $n = 1$ motional Bloch bands. Separate scans are offset in x and y for clarity. (Left) Split line shape for transitions $|g, 0\rangle_q \rightarrow |e, 0\rangle_q$. (Right) The $|g, 1\rangle_q \rightarrow |e, 1\rangle_q$ transition, note the difference in x-axis scale. Separate traces are offset in x and y for clarity with the origin shown as a black line.

different lattice depths across the relevant low lattice regime. At $U/E_r = 63.2$ the linewidth of the transition is Fourier limited by the length of the π-pulse in both cases and the excited state fraction tends towards 100%. As the lattice is lowered we see that the splitting in the upper Bloch band is approximately ten times as large as in the lower band (note the smaller scale in the $n = 0$ plot). The lineshapes are shifted in x and y on the plot for clarity.

The ability to prepare atoms exclusively in higher motional bands is more powerful than simply a tool for probing the Bloch band structure. We have shown that $J_1 \approx 10J_0$. This therefore gives us the ability to change tunnelling in the lattice by an order of magnitude while in essence leaving all other parameters in the lattice unchanged.[12] This provides the ability to access different regimes of J/U than previously thought and has the potential to allow new ways of studying spin-orbit coupling with interaction effects.

[12]In reality some atoms are lost in the process and so the total atom number loaded into the upper Bloch band can never be as high as in the lower band which limits the range of densities that can be explored. Typically $N_1 \lesssim \frac{1}{10} N_0$

5.4 Quasimomentum selection

5.4.1 Quasimomentum dependent state selection

In the Lamb-Dicke regime the ability to resolve the associated detuning of absorbing one quantum of momentum allows us to selectively prepare our atoms in a particular Bloch band. Likewise, the ability to resolve a quasimomentum dependent detuning in weak lattice clock transitions allows us to selectively prepare individual quasimomenta.

By detuning the clock laser frequency to a particular region of the split line profile described in section 5.2, only those atoms in width $\Gamma = 2\pi\Omega$ will be promoted to the excited state. The width is Fourier limited by $\Omega = 2\pi T$ where T is the pulse duration, rather than by the clock laser itself. Due to time variation in the quasimomentum distribution (see section 5.4.2) it is not advantageous to increase T beyond about 10 ms or resolution is lost due to 'blurring' of the distribution. Atoms remaining in the groundstate can be selectively removed from the lattice with a clearing pulse and then those belonging to the desired quasimomentum window can be returned to the groundstate after the clearing pulse and used for measurement.

5.4.2 Bloch oscillations

In order to study the quasimomentum distribution in our 1-dimensional lattice a single quasimomentum "chunk" was prepared in the method described above at $q = q^*$. A finite time τ was allowed to ellapse and then the entire lineshape of the transition from $-1 \leq q/\hbar k_L \leq 1$ was rescanned. Each point in the lineshape requires a separate experimental run. In each sequence the clock laser is first detuned to resonantly promote atoms only at q^* in order to purify the quasimomentum distribution. Then once the atoms are returned to the groundstate, a fixed time τ ellapses and the clock laser is tuned to a second frequency which is varied from shot to shot in order to scan the entire lineshape. This collection of measurements constitutes a single snapshot of the quasimomentum distribution across the Bloch band for the given wait time τ.

We observed that in the case that the 1-dimensional lattice was not aligned perfectly with the horizontal axis that the distribution of quasimomentum in the Bloch band oscillated

through the first Brillouin zone as a function of time. These oscillations are known as Bloch Oscillations [36, 37] and are well understood in the case of solid state system where, for example, an electric field is applied across the sample [38]. The electric field induces a force which is reconciled in the energy band picture by causing a change in quasimomentum over time.

In the case of the periodic potential of the optical lattice, the force which induces the change in quasimomentum is gravity. For a tilted lattice there is a gradient in gravitational potential $\partial U_g/\partial x$ which is felt by the atoms as a force whose effect is to shift the quasimomentum distribution continuously in a single direction. The quasimomentum shifts according to $q(t) = q_0 + \nu_B t \pmod{2\pi}$ where the Bloch oscillation frequency ν_B is given by

$$\nu_B = \frac{Mg \sin\theta_L}{4\hbar k_L} \tag{5.4}$$

As time is increased the distribution is seen to disappear at $+\hbar k_L$ and reappear at $-\hbar k_L$ as it cycles through the first Brillouin zone.

Figure 5.5 shows a series of measurements of the transition lineshape in the first Bloch band at a lattice depth of $U_z/E_r = 11.4$ according to the experimental protocol described above. Here τ is varied from 25 ms to 115 ms and atoms are driven with a Rabi pulse $\Omega = 2\pi\times$ 100 Hz. The red arrow (right inset) shows the detuning of the first pulse which selects quasimomenta in a narrow window around q^*. Due to experimental considerations the shortest possible value of τ is around 25 ms. By $\tau = 25$ ms the quasimomentum distribution has traversed $q/\hbar k \approx 1$ which coincides with the other peak in the density of states and looks inverted from our initial distribution. At $\tau \approx 65$ ms the atoms have completed one cycle of the Brillouin zone and recreate the distribution which was initially prepared.

For the data shown, $\nu_B = 16$ Hz which corresponds to a lattice tilt of $\theta = 16$ mrad. Later in this work we will discuss the dynamics of spin-orbit coupled Fermions in the periodic potential of our optical lattice. In this case it was vital that any residual lattice tilt be eliminated such that $1/\nu_B$ was much longer than experimentally relevant timescales. This was achieved by carefully controlled manipulation of the input and retro mirrors for the optical lattice while observing Bloch oscillations. In this case the lattice tilt was measured to be $\theta \leq 3.5$ mrad which corresponds to $\nu_B \leq 3$ Hz.

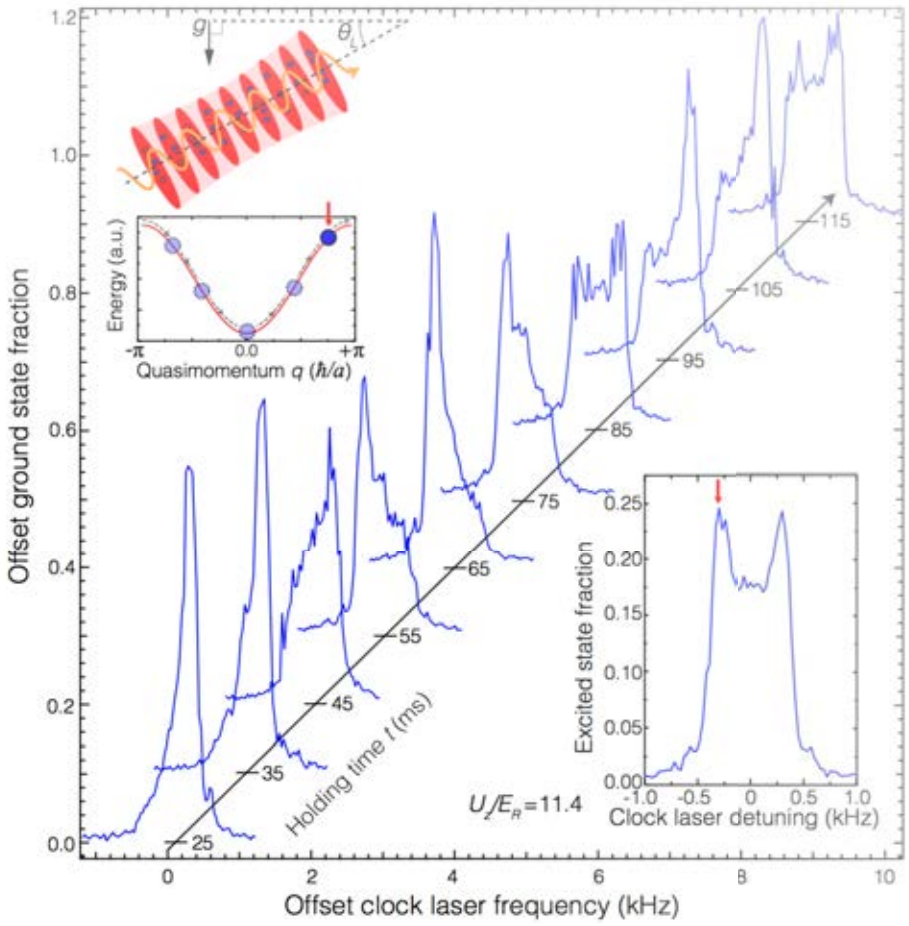

Figure 5.5: Bloch oscillations for a lattice tilt of 16 mRad. The Rabi lineshape is scanned at varying wait times after an initial quasimomentum selecting pulse at q^*. The quasimomentum distribution runs through the first Brillouin zone at an oscillation frequency $\nu_B = 16$ Hz.

5.5 Spin-orbit coupling

5.5.1 Origin of spin-orbit coupling in the lattice

Shifting the $|e,0\rangle$ band with respect to the $|g,0\rangle$ band, as shown pictorially in figure (5.1) is equivalent to analytically shifting the band with a gauge tranformation $|e,q\rangle_n \rightarrow |e,q+\phi\rangle_n$. It can be shown (appendix B) that this allows us to write the atom-light interaction Hamiltonian as

$$H_{SO} = -\hbar \sum_q \vec{B}_n(q,\Omega,\delta)\cdot \vec{S} \tag{5.5}$$

where $\vec{S} = \{S^X, S^Y, S^Z\}$ represents the spin-1/2 angular momentum operators for the ground ($^1S_0$) and excited ($^3P_0$) clock states respectively and $\vec{B}_n(q,\Omega,\delta)$ is an effective mag-

netic field. The dependence of $\vec{B}_n$ on the particular quasimomentum chosen is the origin of the effective spin-orbit coupling exhibited by atoms in the lattice. The vector describing the effective magnetic field is given by

$$\vec{B}_n\big(q,\Omega,\delta\big) = \Big[B_n^X(\Omega), 0, B_n^Z(q,\delta)\Big] \tag{5.6}$$

$$= \left[\Omega, 0, \frac{\big(E_n(q) - E_n(q+\phi)\big)}{\hbar} + \delta\right] \tag{5.7}$$

In the case of flat bands and no spin-orbit coupling, the effective magnetic field is simply the Rabi frequency and points in the X-direction of the Bloch sphere ($\vec{B} = [\Omega, 0, 0]$). For the weak lattice, where the spin-orbit interaction is present, the additional term in the effective magnetic field modifies the dynamics and atoms precess about a new axis which is not confined to the X-direction. In this case $|g, n\rangle$ and $|e, n\rangle$ are no longer eigenstates of the system. The new eigenstates, which we shall label $|-\rangle_q$ and $|+\rangle_q$ exist in the X-Z plane and are characterised by the chiral Bloch angle

$$\theta_{CB} = \tan^{-1}\left(\frac{\Omega}{\frac{1}{\hbar}\big[E_n(q) - E_n(q+\phi)\big] + \delta}\right) \tag{5.8}$$

where δ is the detuning from the true clock transition frequency and we will assume $\delta = 0$ except where explicitly stated. This is the angle between the effective magnetic field and the X axis and it is normal to the circular path which is traversed as atoms transition $|-\rangle_q \rightleftarrows |+\rangle_q$. The new eigenstates can be expressed in terms of the chiral Bloch angle as

$$\begin{aligned}
|-\rangle_q &= \quad \cos\left(\frac{\theta_{n,q}}{2}\right)|g,n\rangle + \sin\left(\frac{\theta_{n,q}}{2}\right)|e,n\rangle \\
|+\rangle_q &= -\sin\left(\frac{\theta_{n,q}}{2}\right)|g,n\rangle + \cos\left(\frac{\theta_{n,q}}{2}\right)|e,n\rangle
\end{aligned}$$

Alternatively we can write the initially polarized states in terms of the true eigenstates $|+\rangle_q$ and $|-\rangle_q$ as

$$\begin{aligned}
|g\rangle_q &= \cos\left(\frac{\theta_{n,q}}{2}\right)|-,n\rangle - \sin\left(\frac{\theta_{n,q}}{2}\right)|+,n\rangle \\
|e\rangle_q &= \sin\left(\frac{\theta_{n,q}}{2}\right)|-,n\rangle + \cos\left(\frac{\theta_{n,q}}{2}\right)|+,n\rangle
\end{aligned}$$

It is worth stressing at this point that the clock laser both drives transitions between the two eigenstates and introduces the spin-orbit coupling. Without the clock laser the eigenstates of the Bloch band are pure $|g\rangle_q$ and $|e\rangle_q$ states. The energies of the two spin-orbit coupled eigenstates are given by

$$E_{n,q,\pm} = \frac{E_n(q) + E_n(q+\phi) + \delta}{2} \pm \left|\vec{B}_n\big(q,\Omega,\delta\big)\right| = \bar{E} \pm \left|\vec{B}_n\big(q,\Omega,\delta\big)\right| \tag{5.9}$$

5.5.2 Spin-orbit dynamics

We can now consider the dynamics in the presence the clock laser (finite Ω). For atoms initially polarized in $|g\rangle_q$ the state evolution is given by

$$\begin{aligned} e^{-i\hat{H}t}|g\rangle_q = &\quad e^{-i(\bar{E}-|\mathbf{B}|)t}\Big(\cos\frac{\theta}{2}|-\rangle_q - \sin\frac{\theta}{2}|+\rangle_q\Big) \\ = &\quad e^{-i(\bar{E}+|\mathbf{B}|)t}\Big(\cos\frac{\theta}{2}|-\rangle_q - e^{-2i|\mathbf{B}|t}\sin\frac{\theta}{2}|+\rangle_q\Big) \\ = &\quad e^{-i(\bar{E}+|\mathbf{B}|)t}\Big(\Big(\cos^2\frac{\theta}{2} + e^{-2i|\mathbf{B}|t}\sin^2\frac{\theta}{2}\Big)|g\rangle_q + \sin\frac{\theta}{2}\cos\frac{\theta}{2}\Big(1-e^{-2i|\mathbf{B}|t}\Big)|e\rangle_q\Big) \end{aligned}$$

for simplicity the indices in $\theta_{n,q}$ are dropped. Additionally, we can consider the expectation value of the operator $\hat{S}^Z$ which tells us how we expect the excitation fraction $n_e = S^Z + 1/2$ to evolve. Using the state evolution we have calculated this is straight forward with $\hat{S}^Z = \frac{\hbar}{2}\left(\begin{smallmatrix}1 & 0\\ 0 & -1\end{smallmatrix}\right)$ and we find

$$\begin{aligned} \Big\langle \hat{S}^Z(t)\Big\rangle =& \frac{1}{2}\Big\{\Big|\cos\frac{\theta}{2}\sin\frac{\theta}{2}\big(1-e^{-2i|\mathbf{B}|t}\big)\Big|^2 - \Big|\cos^2\frac{\theta}{2} + \sin^2\frac{\theta}{2}e^{-2i|\mathbf{B}|t}\Big|\Big\} \\ =& -\frac{1}{2}\Big[\cos^2\big(|\mathbf{B}|t\big) + \cos(2\theta_{n,q})\sin^2\big(|\mathbf{B}|t\big)\Big] \end{aligned}$$

we proceed by noting that $\cos(2\tan^{-1}x) = \frac{2}{1+x^2} - 1$ and therefore we can rewrite the term in $\theta_{n,q}$ using

$$x \to \frac{\Omega}{\frac{1}{\hbar}\big[E_n(q) - E_n(q+\phi)\big] + \delta}$$

and we find

$$\Big\langle S^Z(t)\Big\rangle = -\frac{1}{2}\left[\frac{\frac{1}{\hbar}(\Delta E_n(q,\phi)+\delta)^2 + \Omega^2\cos(|2\mathbf{B}_{n,q}|t)}{\frac{1}{\hbar}(\Delta E_n(q,\phi)+\delta)^2 + \Omega^2}\right] \tag{5.10}$$

where we have introduced $\Delta E_n(q,\phi) = E_n(q) - E_n(q,\phi)$ which is the quasimomentum dependent detuning in absorbing momentum $\hbar k_c$ and $q \to q + \phi$. The evolution of the state populations is that of a detuned Rabi oscillation, albeit, the detuning here arises from the spin-orbit coupling rather than actual detuning of the clock laser. The maximum value of $\langle S^Z \rangle$ and the effective Rabi frequency are given by

$$\langle S^Z \rangle_{\max} = -\frac{1}{2}\frac{(\Delta E_n(q,\phi)+\delta)^2 - \Omega^2}{(\Delta E_n(q,\phi)+\delta)^2 + \Omega^2} \tag{5.11}$$

$$\Omega_{\text{eff}} = \sqrt{\Omega^2 + \left(\frac{1}{\hbar}(\Delta E_n(q,\phi)) + \delta\right)^2} \tag{5.12}$$

We have implicitly assumed a single quasimomentum q and non-interacting atoms in the description so far. The true expectation value of the spin operator is calculated by using a weighted sum over the initial distribution of quasimomentum which has been selected. This approach has been found to very closely approximate the true evolution in the experiment.

5.5.3 Measuring dynamics

The state evolution of the atoms in the lattice can be probed using the methods for excited state fraction counting described in (section 2.6). Atoms are prepared using a pulse with $\Omega = 2\pi \times 10$ Hz in one of five quasimomenta with finite Fourier limited width. The remaining groundstate atoms are removed using a strong clearing pulse. In each case the frequency of the clock laser is then changed to resonance at q^* and a stronger π-pulse ($\Omega = 2\pi \times 100$ Hz is used to drive the atoms. For each of the five initial quasimomentum packets the excited state fraction is then measured as a function of time (figure 5.6). The evolution of the atom population resembles that of a detuned Rabi oscillation, however in this case the effective detuning comes from the spin-orbit coupling. Part b) shows the evolution pictorially on the Bloch sphere where the Chiral Bloch angle is represented by the appropriately coloured vector in the X-Z plane. For clarity the Chiral Bloch angle is plotted separately (inset) across the first Brillouin zone. The dynamics were modelled by theory colleagues [39] and treat the dephasing effect of coupling between the radial and axial modes of the trap perturbatively.

5.5.4 Synthetic gauge fields

In equation 5.5 we saw that the Hamiltonian which describes the atom-light interaction for the spin-orbit coupled atoms can be written as the dot product of an effective magnetic field and a spin component. We will now approach this gauge transformation from a different direction to elucidate the use of the strontium clock as a quantum simulator for strong gauge fields.

We begin by imagining the atoms in our lattice clock as occupying one of the vertices of an N-site ladder (shown in figure 5.7). Each rung on the ladder represents a site in the 1-dimensional lattice m_j. The two legs of the ladder represent the $|g, m_j\rangle_{n,q}$ and $|e, m_j\rangle_{n,q}$ states respectively and form the synthetic dimension. Atoms can move in a synthetic two dimensional space by i) tunnelling from site m to site $m \pm 1$ in real space ii) transitioning $|g\rangle \leftrightarrows |e\rangle$ in the synthetic dimension. This so-called Harper-Hofstadter ladder [40, 41] is in essence a topological extension of the Hubbard model of 1-dimensional lattice physics described earlier where in addition to a hopping rate J in the real dimension we also consider the transition rate Ω in the new synthetic dimension [43].

Since the wavelength (698 nm) of the clock laser is incommensurate with the lattice wavelength (813 nm), each lattice site sees a different phase of the clock beam. The phase difference ϕ is exactly the phase described in section 5.2 where $\phi = \pi\lambda_L/\lambda_c$. Therefore the state evolution of atoms on neighbouring sites differ by a complex phase factor $e^{\pm i\phi}$.

In (figure 5.8) we consider the case of a single plaquette of the Harper-Hofstadter ladder. A particle undergoing a closed loop in our synthetic space given by

$$|g, m\rangle \rightarrow |e, m\rangle \rightarrow |e, m-1\rangle \rightarrow |g, m-1\rangle \rightarrow |g, m\rangle$$

acquires a geometric phase $e^{-i\phi}$. Whereas a particle which travels the same closed path in the opposite direction

$$|g, m\rangle \rightarrow |g, m-1\rangle \rightarrow |e, m-1\rangle \rightarrow |e, m\rangle \rightarrow |g, m\rangle$$

acquires phase $e^{+i\phi}$. For some Hamiltonian, $\hat{H}(x_\mu)$ where $\mathbf{r} = \{x_1, x_2, x_3, \dots\}$ are some set

of physical parameters a geometric phase can arise when the system adiabatically explores a closed loop in parameter space. The geometric phase (also called Berry phase) describes the topology of the parameter space and is separate from the phase factor which the state picks up due to time evolution. The most widely known example is the Aharanov-Bohm phase acquired by a charged particle which traces a closed path around some enclosed magnetic flux. The particle need not directly interact with the magnetic flux to acquire a geometric phase shift, but its effect is nonetheless real and can be measured, for example in a superconducting Josephson junction. In the case of fermions in the 1-dimensional lattice this geometric phase is thought of as a synthetic magnetic flux. This leads to the prospects of exploring Quantum Hall physics using spin-orbit coupled fermions in the optical lattice clock. It also provides an intuitive picture for understanding how the spin-orbit coupled Hamiltonian of the form $\vec{B} \cdot \vec{S}$ arises in which the geometric phase describes a vector potential whose effect is to modify the effective magnetic field of the atom-light interaction.

The synthetic dimension may also allow better understanding of chiral edge currents which are of interest in the study of quantum Hall states [44]. In macroscopic materials Landau orbits caused by the presence of a magnetic field cancel out around the plaquette, except at the edges where chiral edge currents can persist. The Harper-Hofstadter ladder realised in the 1D optical lattice is an analogue system comprised entirely of edge sites and with highly tunable parameters. Making it ideal to probe these effects.

5.5.5 Interactions

The model used above for calculating the dynamics of the spin-orbit coupled fermions in the presence our clock laser assumes non-interacting atoms. In the OLC this is a good approximation. The Pauli exclusion principle prevents atoms on the same site interacting via s-wave collisions. p-wave collision are allowed, and the effects of these higher angular momentum collisions have been studies in the OLC [35]. The p-wave interactions are characterised by scattering volumes b^3_{gg}, b^3_e and b^3_{eg} for the symmetric wavefunctions $|gg\rangle$, $|ee\rangle$ and $(|eg\rangle + |eg\rangle)/\sqrt{2}$. In general p-wave interaction energies are at $\sim {}^1\!/_{10}{}^{\text{th}}$ that of s-wave.

When the tunnelling rate J is sufficiently high, however, we do expect to observe s-wave scattering in the lattice which arises from spin-orbit coupling. An atom tunnelling from

site $m \rightarrow m \pm 1$ can interact with atoms whose internal state varies from its own by phase factor $e^{\pm i\phi}$. It can therefore undergo s-wave collisions which have been 'switched on' by the spin-orbit coupling.

In order to measure these effects we want to employ Ramsey spectroscopy instead of Rabi spectroscopy to analyse the effects [45]. In Ramsey spectroscopy a pulse with Rabi frequency Ω and pulse area $\frac{\pi}{2}$ is used to promote the groundstate atoms to a 50:50 mixture of $|g\rangle$ and $|e\rangle$, thought of as the equator of the Bloch sphere. The atoms are left to precess for some free evolution time τ before a second $\frac{\pi}{2}$-pulse is used to prepare the readout state.

When we make a measurement of the excited state fraction of atoms in our trap we explicitly describe the N-atom distribution. Indeed we collapse this distribution on to the measurement axis: $\{|g\rangle, |e\rangle\}$. However, describing the N-atom collective state on the Bloch sphere should be treated with caution. The intuition of the Bloch sphere as applied to a single two-level atom may not be as readily gained for the many atom state. In general when we treat the N-atom state in the language of the Bloch sphere what we are implicitly doing is considering the net result of N individual atoms precessing individually and describing some vector $\vec{\Psi}$ which describes the sum of all the individual Bloch vectors. For example, in the single atom Bloch sphere the length of the state vector $\vec{\psi_i}$ stays the same throughout the evolution of the system. However, in the N-atom picture $\vec{\Psi}$ can change in length, or have no length whatsoever (if $\sum_i \vec{\psi_i} = 0$). This tells us that the contrast of our final measurement has decreased or is zero.

When considering the effects of interactions we are interested not only in the excited state fraction of our final Ramsey lineshape, but the contrast. When two atoms collide, their Bloch vectors experience a phase shift about the azimuth. When collisional effects build up they result in a reduced contrast in the overall Ramsey lineshape. Additionally, the spin-orbit coupling should modify the density shift of the clock transition as described in [45].

Collisional effects are searched for with the following experimental procedure. The atoms are prepared in a strong lattice and a $\frac{\pi}{2}$-pulse is used to prepare the atoms. The lattice strength is quickly ramped down to the weak confinement regime using the retro lattice

intensity control (discussed in chapter 4) and a free evolution time τ elapses. Finally, the lattice strength is quickly ramped back up to its original strength and the final readout pulse ($\frac{\pi}{2}$) is applied. In this way the atoms spend their free evolution time in the weak periodic potential where tunnelling and s-wave interactions are switched on, but are probed in the strong confinement regime where the transition linewidth is narrower and the resolution is high.

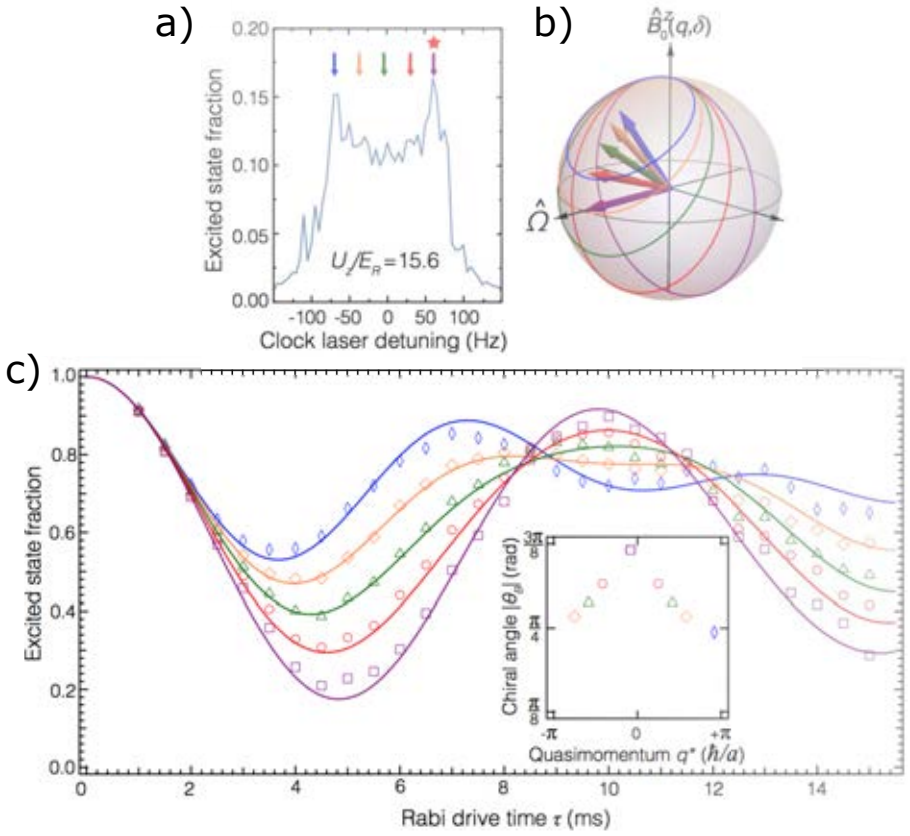

Figure 5.6: Measurements of the Chiral Bloch vector by observation of Rabi state evolution in the lowest motional band. a) five different narrow quasimomenta windows are selected using at the indicated detunings and driven at q^*. b) The atoms evolve by precessing about their Chiral Bloch vector which characterises the spin-orbit coupled eigenstates $|+\rangle_q$ and $|-\rangle_q$. c) The dynamics are measured by recording the excited state fraction in the $|e\rangle$,$|g\rangle$ basis as a function of evolution time. Dephasing of the quasimomentum distribution reduces the contrast with time such that full revival of the initial state is not seen.

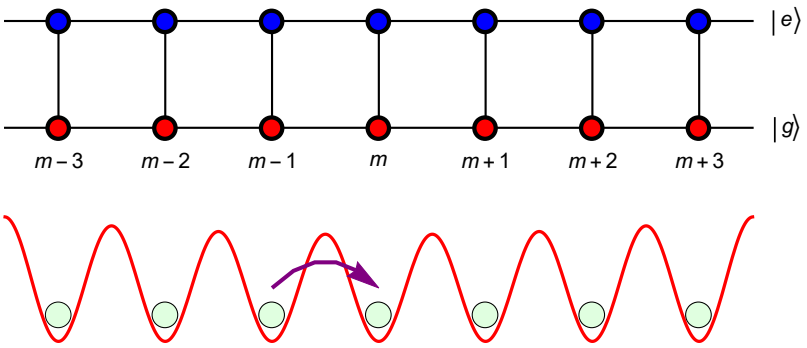

Figure 5.7: The clock state in the 1D optical lattice can be thought of as a synthetic dimension, with atoms moving in a pseudo 2D array of sites described by the Harper-Hofstadter 'ladder' Hamiltonian. Atoms tunnel in the real dimension with rate J and transition between the ground/excited state at rate Ω.

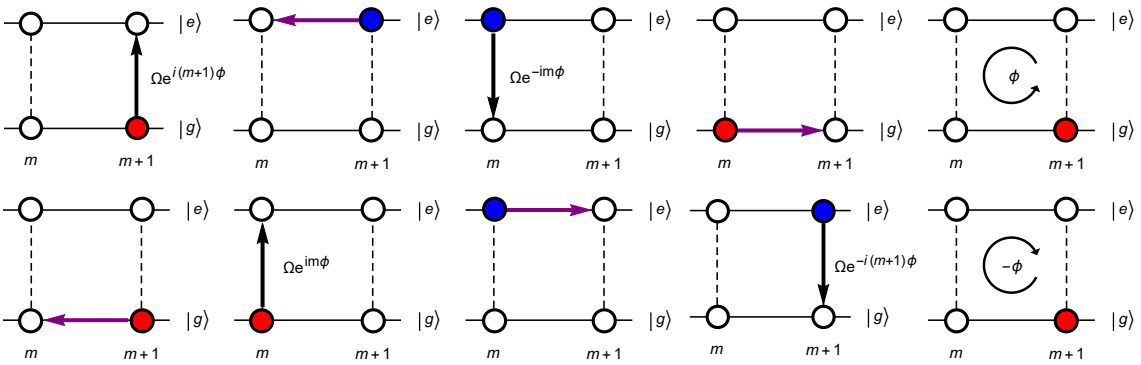

Figure 5.8: An atom moving around a single plaquette of the Harper-Hofstadter ladder acquires a geometric phase $\pm\phi$ due to the difference in clock phase between sites m and $m+1$. An atom travelling anti-clockwise (top) and clockwise (bottom) see a phase difference with opposite sign. This can be thought of as arising from a synthetic gauge field.

6 Conclusion

In this thesis I have discussed the utility of the strontium optical lattice clock as a quantum simulation tool. The confining, periodic potentials of the optical lattice which are necessary to freeze out recoil Doppler motion from the clock transition, also represent an interesting environment in which to observe atoms. Using the clock to study synthetic spin-orbit coupling, first proposed by theory colleagues at JILA [45], is a novel way to study such effects which are of direct interest to those in the solid state community.

I have given an overview of progress on the strontium atomic lattice clock to date and details the motivations for i) improving intensity stablity via negative feedback control ii) introducing the ability to ramp the lattice intensity to probe weak lattice physics. I have detailed the design and characterisation of the intensity servo I worked on and suggested possible improvements for future systems.

In the weak lattice, the Bloch band structure of the electronic quasi-motion becomes apparent. Using the ultra-narrow spectroscopy available using the clock laser/transition, we can resolve a quasimomentum dependent detuning in the clock transition. We have used this tool to study Bloch oscillations in the tilted lattice and to show that synthetic spin-orbit coupling modifies the dynamics of Rabi oscillations by the creation of two q-dependent energy eigenstates $|+\rangle$ and $|-\rangle$.

On going work is being conducted to introduce interactions into the spin-orbit coupling picture by varying the fundamental parameters U, J and Ω and using Ramsey spectroscopy to map collisional phase changes on to the $|e\rangle$, $|g\rangle$ state space. Better understanding of these interactions will not only lead to better understanding of systematics in the clock itself, but to analogue systems such as strongly correlated metal phases in Kondo lattices [48].

7 Outlook

Alongside the work detailed in this thesis, efforts are under way to push the strontium optical clock towards a new era of performance. The main areas of active research at JILA are detailed in brief below:

- **Silicon Reference Cavity** The current generation of clock laser relies on a 40 cm reference cavity using a ULE spacer and amorphous dielectric mirrors. It has been shown [15] that the clock laser performs at the thermal noise floor of the cavity which is fundamentally limited by material choice. In addition, the amorphous nature of the materials leads to linear frequency drift due to material creep.

  Recent advances have been made by choosing crystalline materials for the spacer [49] (and soon the mirrors). Crystal materials have well defined intrinsic directionality and structure and can be cut to reduce susceptibility to vibration. They should also exhibit almost no material creep. In addition, by choosing a high Young's modulus material, thermal noise susceptibility is reduced. The thermal expansion coefficient of Silicon has a zero crossing at ∼4 K and ∼124 K. By operating at these points length noise due to thermal fluctuations is almost eliminated.

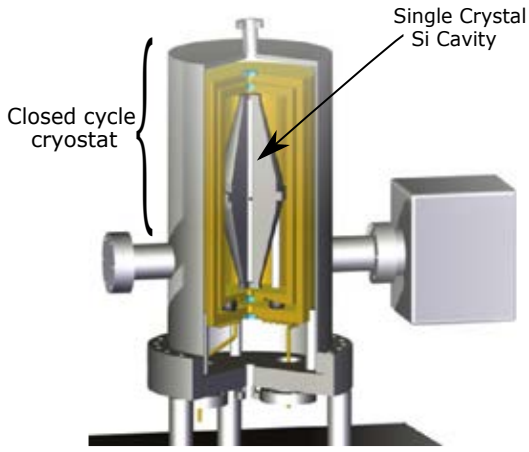

Figure 7.1: JILA Si Cavity design shown inside heat shields and vacuum. A closed cycle Montana Instruments cryostat controls the temperature to 124 K using liquid Nitrogen.

Additionally, crystalline mirrors can be used to reduce thermal noise in the coatings. It is thought that with these improvements the stability of the cavity can reach the theoretical thermal noise floor of 4×10^{-17}, and linear drift rates on the order of $\sim$mHz/s have already been observed.

- **3D Optical Lattice** The sister experiment to Sr1 is the Sr2 (often called SrQ) experiment. This machine has been recently modified to operate a 3D Fermi degenerate gas. This can be utilised to prohibit double occupation on lattice sites. Due to the higher number of distinct lattice sites available in the 3D lattice configuration the $\sqrt{N}$ advantage in clock performance can still be large while effectively eliminating density shifts.

  One difficulty is that it is not possible in 3 dimensions to align $\vec{k}\cdot\vec{B}$ in all axes to cancel the vector component of the atomic Stark shift induced by the lattice beams. The Sr2 team have recently achieved a low entropy ($T/T_f = 0.2$) Fermi degeneracy gas of strontium atoms and demonstrated a record atom light coherence of $Q = 5\times10^{15}$ with 1×10^4 atoms [50]. They have also carried out a systematic evaluation of the magic wavelengths for the two horizontal and one vertical lattice beams and proven that contact interactions in the lattice can be resolved spectroscopically, therefore reducing their contribution to systematic uncertainty in the clock.

  It is as yet unclear how to utilise such a large atom-light coherence time to facilitate better metrology. At the present level of clock laser performance the Dick Effect (where high frequency clock noise is aliased between clock duty cycles) will in fact reduce the 3D lattice clock performance below presently reported levels. However, improvements in the clock laser will reduce the Dick Effect, and modified clock protocols may ultimately allow the benefits of 3D to shine through.

- **Spin-Squeezing** By interrogating many thousands of atoms, neutral atom clocks achieve a $1/\sqrt{N}$ systematic improvement over their ion counterparts which stems from the Poissonian nature of the atomic projection noise inherent in the state measurement technique described in section 2.6. This limit is, however, not fundamental. It has been proposed [51] that squeezing of the spin-quadrature can be achieved in the clock, leading to a sub-Poissonian uncertainty in state counting. By squeezing the spin quadrature a Heisenberg limited enhancement factor of $1/N$ is theoretically possible.

  Future work on the Sr1 experiment hopes to realise a spin-squeezed optical lattice

clock using an in-vacuum high finesse cavity. Benefitting from the $1/N$ boost by using a cavity to develop phase squeezing, which can be rotated around the Bloch sphere to create a reduction in the spin quadrature.

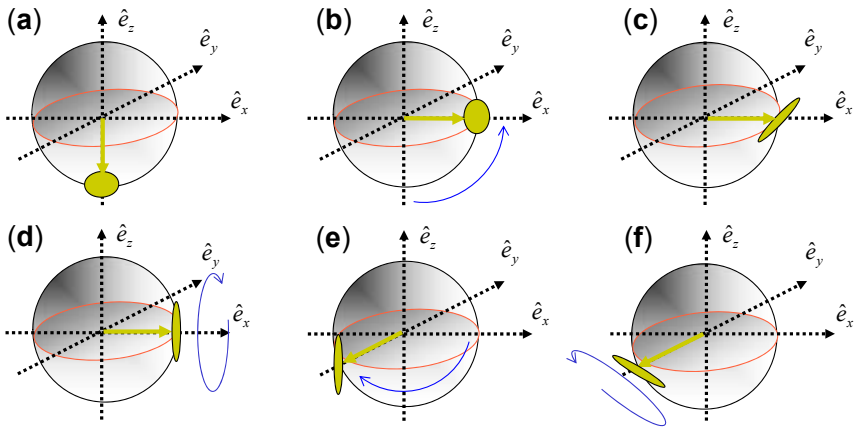

Figure 7.2: Protocol for creating a spin squeezed entangled state. A phase squeezed state (for example created via a cavity) can be mapped on to the measurement axis via a rotation pulse about $\hat{e}_x$. (Image from [51])

References

[1] S. Kolkowitz, S. Bromley et. al."Spin-Orbit Coupled Fermions in an Optical Lattice Clock", Nature **542** 66-70 (2016)

[2] W. Thomson and P. G. Tait, Elements of Natural Philosophy, Cambridge: At the University Press, p. 61-62 (1879).

[3] Comptes Rendus de la 13e CGPM (1967/68), 1969, p.103

[4] J. C. Hafele, R. E. Keating "Around-the-world Atomic Clocks observed relativistic time gains" Science, Vol. 177, No. 4044 pp. 168-170 (1972)

[5] C. W. Chou et. al. "Frequency comparison of two high-accuracy Al^+ optical clock" Phys. Rev. Lett. **104**(7) 070802 (2010)

[6] S.Kolkowitz et. al. "Gravitational wave detection with optica lattice atomic clocks" Phys. Rev. D. **94** 124043 (2016)

[7] A. Arvanitaki et. al. "Searching for dilaton dark matter with atomic clocks" Phys. Rev. D. **91**, 015015 (2015)

[8] A. Derevianko, and M. Pospelov "Hunting for topological dark matter with atomic clocks" Nature Physics **10** 933 (2014)

[9] S. Blatt et. al. "New limits on the coupling fundamental constants to gravity using ^{87}Sr optical lattice clocks" Phys. Rev. Lett. **100**(14) 140801 (2008)

[10] V. V. Flaubaum et. al. "Search for variation of the fundamental constants in atomic, molecular and nuclear spectra" Canadian Journal of Physics, **87**(1), pp. 25-33 (2009)

[11] R. P. Feynmann "Simulating Physics with Computers" Internation Journal of Theoretical Physics, Vol. 21, 6-7, pp. 467-488 (1982)

[12] A. D. Ludlow "The Strontium Optical Lattice Clock: Spectroscopy with Sub-Hertz Accuracy" Ph.D Thesis, University of Colorado (2008)

[13] M. M. Boyd "High Precision Spectrscopy of Strontium in an Optical Lattice: Towards a new Standard for Frequency" Ph.D Thesis, University of Colorado (2007)

[14] S. Blatt "Ultra-cold collisions and fundamental physics with Strontium" Ph.D Thesis, University of Colorado (2011)

[15] M. J. Martin "Quantum Metrology and Many-Body Physics: Pushing the Frontier of the Optical Lattice Clock" Ph.D Thesis, University of Colorado (2013)

[16] M. N. Bishof "Understanding Atomic Interactions in an Optical Lattice Clock and using them to study Many-Body Physics" Ph.D Thesis, University of Colorado (2014)

[17] T. Esslinger "Fermi-Hubbard Physics with atoms in an optical lattice" *arxiv: 1007.002* (accessed 04/07/17)

[18] P. W. Anderson "The resonating valence bond state in La_2Cu0_4 and superconductivity" Science, **235** pp.1196-98 (1987)

[19] L.-S. Ma, P. Jungner, J. Ye, and J.L. Hall. "Delivering the same optical frequency at two places: accurate cancellation of phase noise introduced by an optical fiber or other time-varying path" Optics Letters, **19**:1777–1779, 1994

[20] S.M. Foreman, A.D. Ludlow, M.H.G. de Miranda, J.E. Stalnaker, S.A. Diddams, and J. Ye. "Coherent optical phase transfer over a 32-km fiber with 1 s instability ¡ 1017" Phys. Rev. Lett. **99**:153601 (2007)

[21] K. R. Vogel et. al. "Narrow line Doppler cooling of Strontium to the recoil limit" IEEE Transactions on Instrumentation and Measurement **48**(2) (1999)

[22] R.H. Dicke "The effect of collisions upon the doppler width of spectral lines" Phys. Rev. 89, 472 (1953)

[23] T. Ido, H. Katori "Recoil-Free Spectroscopy of Neutral Sr Atoms in the Lamb-Dicke Regime" Phys. Rev. Lett. **91**, 053001 (2003)

[24] M. Bishof, X. Zhang, M. J. Martin, J. Ye "Optical Spectrum Analyzer with Quantum-Limited Noise Floor" Phys. Rev. Lett. **111**, 093604 (2013)

[25] S.A. Diddams, J.C. Bergquist, S.R. Jefferts, and C.W. Oates. "Standards of time and frequency and the outset of the 21st century" Science **306**:1318–1324 (2004)

[26] F. Quinlan et. al. "Exploiting shot noise correlations in the photodetection of ultrashort optical pulse trains" Nature Photonics **7**, 290–293 (2013)

[27] G. Morigi "Laser cooling of two trapped ions: Sideband cooling beyond the Lamb-Dicke limit" Phys. Rev. A. **59**(5) (1999)

[28] D. Leibfried, R. Blatt, C. Monroe, D. Wineland "Quantum dynamics of single trapped ions" Rev. Mod. Phys. Vol. 75 (2003)

[29] R. Grimm, M. Weidermüller, Y. B. Ovchinnikov "Optical dipole traps for neutral atoms" Advances in Atomic, Molecular and Optical Physics, **42** pp. 96-170 (2000)

[30] J. D. Jackson "Classical Electrodynamics" (1962)

[31] H. Katori et. al. "Ultra-stable optical clock with neutral atoms in an engineered light shift trap" Phys. Rev. Lett. **91**(17) 173005 (2003)

[32] T. L. Nicholson "A new record in atomic clock performance" Ph.D Thesis, University of Colorado (2015)

[33] N. W. Ashcroft, N. D. Mermin. "Solid state physics" Saunders College Publishing, Fort Worth, TX (1976)

[34] N. D. Lemke, J. von Stecher, J. A. Sherman, A. M. Rey, C. W. Oates, and A. D. Ludlow, "p-Wave cold collisions in an optical lattice clock," Phys. Rev. Lett., vol. 107, no. 103902 (2011)

[35] M. J. Martin, Bishof, M. , Swallows, M. D. , Zhang, X. , Benko, C. , von-Stecher, J. , Gorshkov, A. V. , Rey, A. M. , and Ye, J. "A Quantum Many-Body Spin System in an Optical Lattice Clock" Science, vol. 341, no. 6146, pp. 632 - 636 (2013)

[36] A. R. Kolovsky, H.J. Korsch "Dynamics of interacting atoms in driven tilted optical lattices" J. Sib. Fed. Univ. Math. Phys. **3**(3) pp. 311-324 (2010)

[37] Dahan, M. B., Peik, E., Reichel, J., Castin, Y. Salomon, C. "Bloch oscillations of atoms in an optical potential" Phys. Rev. Lett. **76** 4508 (1996)

[38] T. Dekorvsky et. al. "Bloch oscillations at room temperature" Phys. Rev. B **51**, 17275 (1995)

[39] S. Kolkowitz, S. Bromley et. al."Spin-Orbit Coupled Fermions in an Optical Lattice Clock" - *Additional Material*, Nature **542** 66-70 (2016)

[40] Hugel, D. Paredes, B. "Chiral ladders and the edges of quantum Hall insulators". ¨ Phys. Rev. A **89**, 023619 (2014)

[41] M. Aidelsburger, et al. "Realization of the Hofstadter Hamiltonian with ultracold atoms in optical lattices" Phys. Rev. Lett. **111**, 185301 (2013)

[42] Miyake, H., Siviloglou, G. A., Kennedy, C. J., Burton, W. C. Ketterle, W. "Realizing the Harper Hamiltonian with laser-assisted tunneling in optical lattices" Phys. Rev.Lett. 111, 185302 (2013)

[43] A. Celi, et al. "Synthetic gauge fields in synthetic dimensions" Physical Review Letters **112**, 043001 (2014)

[44] M. Mancini et al. "Observation of chiral edge states with neutral fermions in synthetic Hall ribbons" Science 349, 1510–1513 (2015)

[45] M. Wall et. al. "Synthetic Spin-Orbit Coupling in an Optical Lattice Clock" Phys. Rev. Lett. **116**, 035301 (2016)

[46] N. Darkwah-Oppong "Towards a quantum degenerate fermi gas of strontium-87 in a 3D optical lattice" Masters Thesis, ETH Zurich Department of Physics (2015)

[47] M. Greiner "Ultracold quantum gases in three-dimensional optical lattice potentials" Ph.D Thesis, LMU Munich (2003)

[48] L. Isaev, J. Schachenmayer, and A. M. Rey "Spin-orbit coupled correlated metal phase in Kondo lattices: an implementation with alkaline-earth atoms" Phys. Rev. Lett. **117**(13) 135302 (2016)

[49] T. Kessler, C. Hagemann et. al. "A sub-40 mHz linewidth laser based on a silicon single-crystal optical cavity" Nature Photonics **6**, 687–692 (2012)

[50] S.L. Campbell, R.B. Hutson, G.E. Marti, A. Goban, N. Darkwah Oppong, R.L. McNally, L. Sonderhouse, J.M. Robinson, W. Zhang, B.J. Bloom, J. Ye "A Fermi-degenerate three-dimensional optical lattice clock" *arXiv:1702.01210* (accessed 04/07/17)

[51] Polzik, S. E., Ye, J., (2015) "Entanglement and squeezing in a network of distant optical lattice clocks", Phys. Rev. A **93**, 012404 (2016).

Appendices

A Generating arbitrary feedforward ramps

In the text we discussed how the non-linearities of the actuator in the intensity stabilisation scheme (primarily due to the double balanced mixer and AOMs) could be modelled to allow a 'feed-forward' signal to be produced of the form

$$F_V(t) = \frac{1}{k_1}\left[\ln\left[\frac{2P_0}{\pi}\sin^{-1}\left(\frac{I_R(t)}{I_0}\right)^{-\frac{1}{8}} - 1\right] + V_{1/2}\right]$$

which allows us to generate an arbitrary intensity ramp $I_R(t)$ which very closely approximates the desired set point. This means the servo error is kept small and the feedback is more stable. Below are some of the ramps/feedback curves calculated using Mathematica and used to program the DAQ.

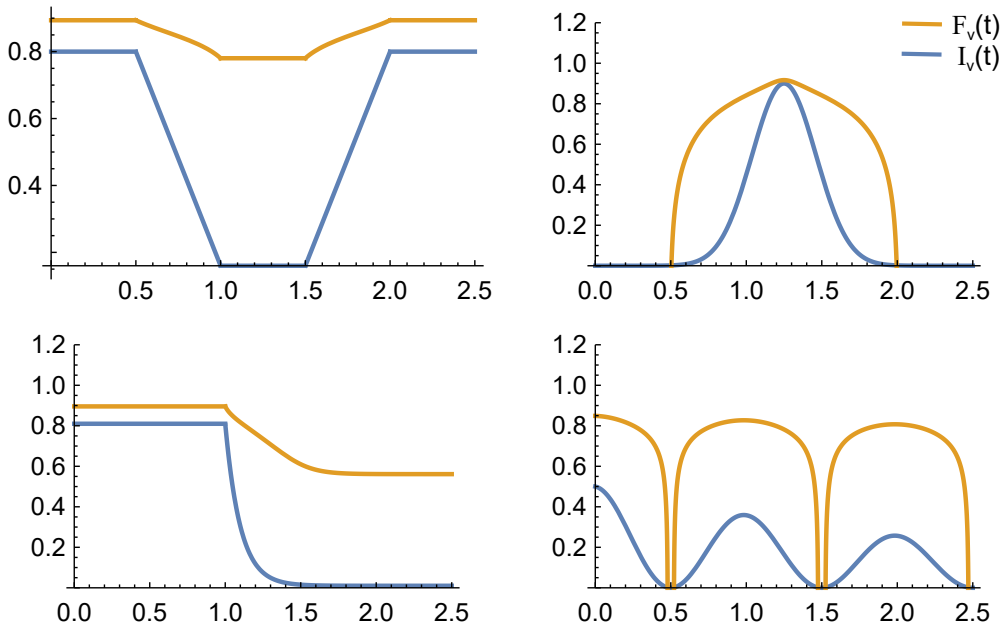

Figure A.1: Examples of the feed forward process. The laser intensity is ramped according to a prescribed path (blue). Due to the non-linearities, this requires the controller to output the feed forward function $F_v(t)$.

B Writing atom-light interaction in $\vec{B} \cdot \vec{S}$ form

The full Hamiltonian for clock photons interacting with trapped atoms in band n, with initial quasimomentum q, in electronic state $\alpha = \{+, -\}$ and where $\phi = \pi \frac{k_c}{k_L}$ is given by:

$$\hat{H}_n^0 = \sum_{q,\alpha} E_{\alpha,n,q} \hat{n}_{\alpha,n,q} - \sum \left[\frac{\Omega_n}{2} \hat{a}^\dagger_{+,n,q+\phi} \hat{a}_{-,n,q} + h.c. \right] \tag{B.1}$$

where $\hat{a}^\dagger$, $\hat{a}$ and $\hat{n} = \hat{a}^\dagger \hat{a}$ have their usual meaning and represent atoms being promoted/demoted between electronic states. If we employ a gauge transformation $q \to q + \phi$ we can diagonalise the Hamiltonian in the angular momentum space (in the text we do this explicitly by translating the two bands as a visual aide - figure 5.1). We can now write our atom-light interaction Hamiltonian in the form

$$\hat{H}_n^0 = \sum_{q,\alpha} \vec{B}_{n,q} \cdot \vec{S}_{n,q} \tag{B.2}$$

where $\vec{S}^{X,Y,Z} = \frac{\hbar}{2} \hat{\sigma}^{X,Y,Z}$ where $\hat{\sigma}^i$ are the spin 1/2 Pauli matrices. We therefore would write

$$\hat{H}^0_{n,q,\alpha} = \begin{pmatrix} \Delta E_n(q,\phi) + \delta & \Omega_n \\ \Omega_n^* & -(\Delta E_n(q,\phi) + \delta) \end{pmatrix} \tag{B.3}$$

where $\Delta E(q,\phi) = E_n(q) - E_n(q+\phi) \approx 2J_n[cos(q) - cos(q+\phi)]$ is the quasimomentum detuning due to band width and δ has the same meaning as in the text.

C Approximating Bloch bands as sinusoidal

As stated in the text, for a suitably deep lattice potential the band structure is well approximated by

$$\Delta E^{(0)}_{q,\sigma} = E^{(0)}_{0,\sigma} - 2\hbar J \cos(\hbar q)$$

Shown below is the $n = 0$ Bloch band for 6 lattice depths. The Bloch band calculated using the method discussed in 3.3.2 (blue) and the sinusoidal approximation (yellow) are shown.

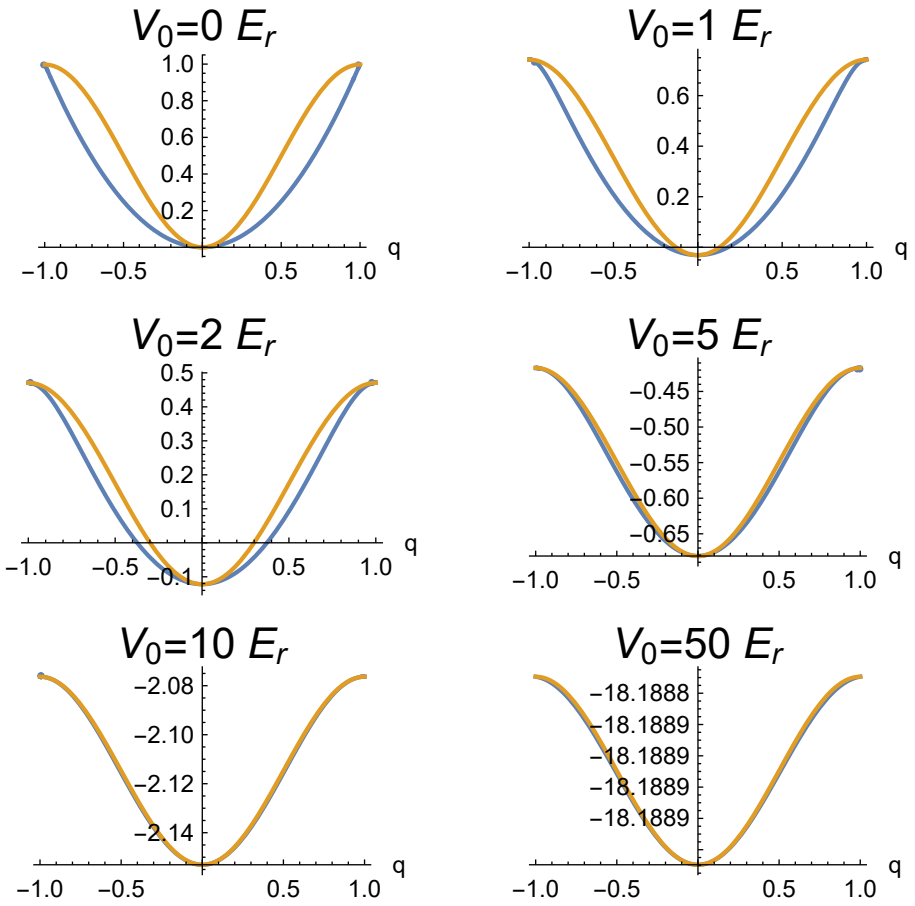

Figure C.1: (Blue) Tri-diagonal matrix solution for $n = 0$ Bloch band and (Yellow) sinusoidal approximation for lattice depths $0 \rightarrow 50$ E_r.

D Intensity servo schematic

JILA Intensity Servo Controller